International Journal of Progressive Sciences and Technologies (IJPSAT)
ISSN: 2509-0119.

http://ijpsat.ijsht-journals.org
Vol. 22 No. 2 September 2020, pp. 87-110

# *Assessment of Banded Iron Formations around Gouap Area as Potential High-Grade Iron Ore (Nyong Serie, Congo Craton - South Cameroon)*

Ndema Mbongué Jean-Lavenir [1, 2], Mbonjoh Terence Manachi [1]

[1] Department of Geology, University of Buea; Buea, Cameroon

[2] Laboratory of Petrology and Structural Geology, Department of Earth Sciences, Faculty of Sciences, UY I,



**Abstract – The Gouap area is found in the southern part of Cameroon and belongs to the Nyong Series situated NW corner of the Ntem Complex. The assessment of banded iron formations (BIFs) in this area is carried out through rock sampling survey. Samples were analyzed by inductively coupled plasma mass spectrometry (ICP-MS) combined with instrumental neutron activation analysis (INAA) technologies to completely characterize the rocks. The studied banded iron formations show microband texture and granoblastic microstructure. The mineral assemblage indicates that they undergone the metamorphism of greenschist facies conditions. The chemical composition of the Gouap iron formations shows that the major components (99.43%) that are $Fe_2O_3$ and $SiO_2$ indicate the purity of the chemical precipitates. The Gouap iron deposits fall into the group of oxide facies with magnetite as dominant mineral and the most diagnostic fingerprints of the source metals are Ni, Cr and Cu. The Gouap iron deposit displays some light terrigenous input in its geochemistry implying that it belongs to the Algoma- type and indicates that iron formations were deposited in an environment devoid of siliciclastic detrital input. The Gouap BIFs derived from Precambrian mature quartz arenite and Fe-sand that were deposited in an Oceanic Island-arc Margin (ARC) setting under oxic conditions with slow sedimentation accompanied with minor input of anoxic conditions with fast sedimentation. This constitutes a new result for de iron deposits in Cameroon. The overall data of Gouap iron deposits pointing to hydrothermal and Red Sea hydrothermal deposits (RS). They exhibit Low- temperature hydrothermal fluids (< 0.1%) and Seawater, indicating that mixing of seawater and less amount (< 0.1%) of low-temperature hydrothermal fluids (< 200°C) might have occurred during their deposition. Some samples have values that reflect between 1 to 5% of a high-temperature hydrothermal fluid input suggesting that the Gouap iron formations were deposited close to the distal position. The high concentration of $Fe_2O_{3(T)}$ in the Gouap iron deposit (average = 63.73 wt%) shows that it has a very interesting potential for exploitation and this iron contents can be classified as high- grade or medium- grade iron ores by global standards, and it fall within the acceptable levels for commercial ores. Gouap BIFs host high- grade siliceous ore with magnetite being the predominant mineral. This also constitutes a new result for the iron deposit in Cameroon.**

**Keywords – Gouap Area, Microband Texture, Precambrian, Distal Position, High- Grade Siliceous Ore.**

## I. INTRODUCTION

Banded iron formations (BIFs) are iron- rich and siliceous chemical sedimentary deposits that precipitated from seawater throughout much of the Archaean and Palaeoproterozoic (3.8–1.85 Ga), with the major element composition dominated by $SiO_2$ (40–60 wt. %) and Fe (15–40 wt. % $Fe_2O_3$), and minor amount of $Al_2O_3$, MgO, CaO, $K_2O$, $Na_2O$, and $P_2O_5$ [1, 2, 3]. They are more often than not, laminated, with banding observed on a wide range of scales, from coarse macrobands (meters in thickness) to the characteristic mesobands (centimeter-thick units) by which they are typically defined to microbands (millimeter to submillimeter). The mineralogy of BIFs from the best-

**Corresponding Author:** Ndema Mbongué Jean-Lavenir

preserved sequences is remarkably uniform, comprising mostly chert, magnetite, hematite, Fe- rich silicate minerals (stilpnomelane, greenalite, mines otaite, and riebeckite), carbonate minerals (siderite, ankerite, calcite, and dolomite), and minor sulfides (pyrite and pyrrhotite [4]). Toward the end of Archaean, the marine depositional setting for BIF formation changed from depositional basins with rapid thermal subsidence and deposition of large volume of interbedded volcanic and volcanogenic graywackes [5, 6], to a more stable style of sedimentation in extensive shallow marine basins along stable continental platforms [7, 8, 9]. BIF deposited in the former setting are considered Algoma- type, whereas BIF formed in the latter setting are Superior- type.

BIFs, widely regarded as chemical/biochemical sediments that precipitated from ocean water have their rare earth element (REE) distribution widely used as geochemical proxy to provide insight into the ocean water chemistry [10] and life [11] at the time of their deposition. They are of great interest due to their economic importance as the world's largest source of iron ore [12], and because the models proposed to explain their genesis are intimately linked to the evolution of the earth's atmosphere, hydrosphere, and biosphere [13, 14]. Secular changes in their accumulation and sedimentary style continue to motivate efforts to understand their origins. However, detailed reviews of their characteristics and proposed depositional models are readily available [1, 2, 15]. What stands out of these characteristics are their limited occurrence in time (3.8–1.8 Ga and 750 Ma) and evolving stratigraphic settings through time.

The largest accumulations of iron formation (IF) were deposited between 2.7 and 2.45 Ga ago [2, 16], before the rise of atmospheric oxygen also known as Great Oxidation Event (GOE) after [17] by 2.32 Ga ago. However, recent studies show that a transient atmospheric oxygenation event occurred at least 0.6 Ga prior to the GOE [18]. Until 1.8 Ga, the oxygenation of the atmosphere and the development of a sulfidic deep ocean led to the cessation of the BIF deposition [1, 19, 20, 21]. Then, major iron formations did not reappear until the late Neoproterozoic era due to a 0.7 Ga snowball event which radically changed the chemistry of the global ocean [2, 22]. Due to the special depositional setting, the BIFs are commonly used as a clue to understand the evolution of the Precambrian blocks [23, 24, 25, 26]. However, the deposition of the older greenstone belt– hosted (3.8–2.5 Ga) and craton margin (3.0–1.8 Ga) BIFs, especially before the GOE: 2.45–2.32 Ga [17, 27], is more challenging to explain.

During the period of BIFs deposition, the oceans (at least at depth) were anoxic and sulfur poor (at least at depth), thus capable of transporting and accumulating dissolved ferrous iron [28, 29]. The latter may have been oxidized to solid-phase iron oxyhydroxides through either biological (oxygenic or anoxygenic photosynthesis) or nonbiological (ultraviolet photo-oxidation) processes [30]. Alternatively, direct precipitation under anoxic conditions may have formed Fe- carbonates or mixed valence Fe- silicates. Based on REE distributions, it has been proposed that Fe and Si in most BIFs derive from hydrothermal sources [29, 31], although [32] used Ge/Si ratios in BIFs to postulate a continental source for silica.

Hagemann et al. (2016) suggested that a BIF with an average of about 30–35% Fe is the necessary prerequisite for the formation of a significant high-grade (> 55% Fe) BIF-hosted deposit. However, the processes responsible for the upgrade of the BIF protore to high- grade iron ore are still unclear. Two end-member epigenetic models have been proposed for the enrichment of a BIF protore: (i) the supergene enrichment model involves the selective leaching of gangue minerals from the BIF by ground-water and the residual accumulation of the iron oxides; (ii) the hypogene enrichment process is ascribed to the interaction of the BIFs with a hydrothermal fluid, which dissolves chert (quartz), leaving pore spaces that were partly filled by a new generation of iron oxides associated with carbonates, iron silicates, and apatite [34, 35]. An alternative third epigenetic model proposes the hypogene–supergene-modified origin. This model comprises two stages of iron enrichment: an initial hypogene stage with either leaching of all the chert from the BIF protore, leaving pore spaces, or with metasomatic replacement of those minerals by carbonates followed by a supergene stage that leached the hydrothermal minerals formed in the previous stage [34, 36].

Precambrian banded iron formations are the most important type for iron resources in the world and extraordinary chemical marine sediments formation only occurred in the early Earth, which were concentrated during Archaean to Early Proterozoic eras (3.2 – 1.8 Ga). In Cameroon, BIFs are mainly distributed in the Archaean to Palaeoproterozoic Ntem Complex greenstone belt. With the increasing global demand for iron since the last decade, the Ntem Complex has become more attractive for mineral exploration. The reconnaissance exploration program of Bureau de Recherche Géologique et Minière (BRGM) recognized high magnetic signatures in the Mbalam, Nkout, Bikoula, Meyomessi, Ngovayang and Mewongo. Morever research studies related to BIFs have also been carried out in the Ntem complex greenstone belt notably in Metzimevin

[37]; Mbalam [38, 39, 40]; Nkout [38, 41]; Meyomessi [42]; Njweng [43]; and Bikoula [44] areas. In addition, many iron-rich bodies are also reported in the Nyong Series such as Elom [45], Zambi area [46], Kouambo [47] , Kpwa-Atog Boga [48], Gouap [49, 50], Messondo [51], Kelle Bidjoka [52], Bipindi [53], Bienkop [54], Kopongo [55], Pout Njouma [56]. The other iron occurrences have been found in the Pan-African formations like Mayo Binka [37], Mafé [57], Touboro and Vaimba in the Adamawa Region. The aim of this work is to study the petrography and geochemical characteristics of the Gouap iron occurrence and investigate for the grade of iron ore mineralization.

## II. Geological Setting

The Gouap area is located within the Ntem Complex (northwestern margin of the Archaean Congo Craton in Cameroon), bordered in the north by the Yaoundé Series [58] of the Pan-African orogenic belt in Central Africa (Fig. 1a, 1b). The Ntem Complex is predominantly made up of Archaean rocks that were partially reworked during the Palaeoproterozoic–Transamazonian and Pan-African–Braziliano cycles [59, 60, 61, 62, 63]. This Precambrian basement of southern Cameroon experienced a thermotectonic evolution accompanied with the emplacement of ferriferous formations also known as band iron formations (BIFs) or itabirites, and the Banded iron formation being the subcrustal formations which form the greenstone belt [64]. The Ntem BIFs consist of oxide-facies and silicate-facies BIF, which are spatially associated with different wallrock types such as gneiss, quartzite, schist, amphibolite, syenite, and rarely epidotite–serpentinite [37, 41, 42, 43, 44, 47, 48]. The majority of these BIFs have undergone a greenschist to granulite facies metamorphic grade, where significant banded iron formations- hosted iron deposits have been discovered [44, 47]. The Ntem complex is subdivided into two main units: the Ntem unit and the Nyong unit.

The Ntem unit is dominated by plutonic rocks of the charnockite suite and by intrusive tonalites, trondhjemites and granodiorites (TTG), dated at 2.9 Ga [59, 66, 67]. The Gouap area is found within the Nyong unit. The Nyong unit is located in the NW corner of the Congo craton and constitutes the main Paleoproterozoic unit in Cameroon, it is a well-preserved granulitic unit of the West Central African Belt resting as an Eburnean nappe on the Congo craton [59, 67, 68]. The works of [69] reveal that the Nyong unit consists of metasedimentary and metavolcanic rocks, syn-to late-tectonic granitoids and syenites. The other lithologies encountered in the Nyong unit include: metamorphosed mafic–ultramafic rocks, expressed as pyroxenites and amphibolites [70], orthogneisses and metaquartzites with a dominance of biotite–amphibole–gneiss, pyrigarnite and magnetite-bearing gneiss [40]. The main plutonic rocks include syn- to late-tectonic charnockites, alkaline syenites and post-tectonic metadiorites [59, 68].

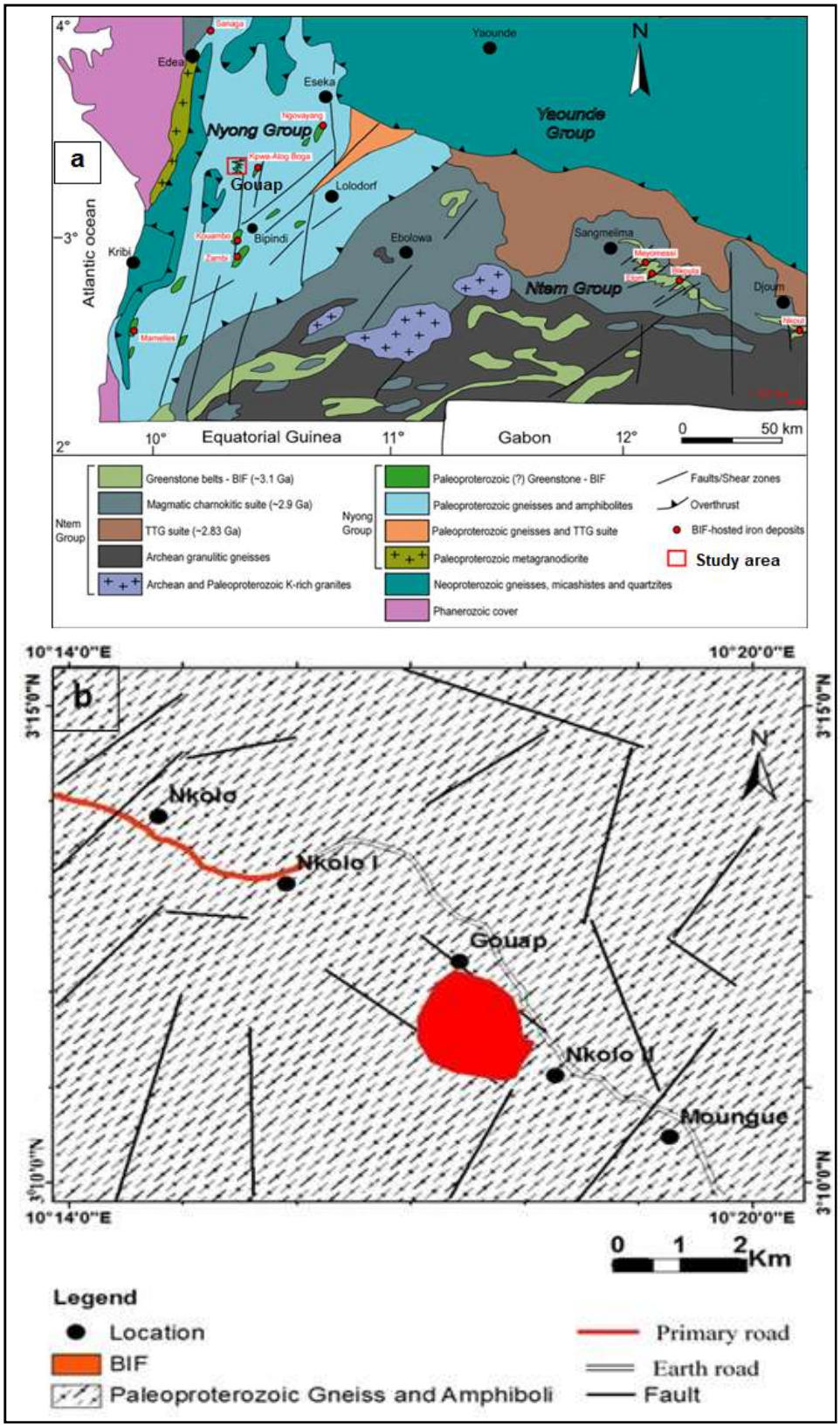


Figure 1. (a) Geological map of SW Cameroon [65] as modify from [50] showing the location of the Gouap iron deposit; (b) Geologic map of the study area.

## III. Methods Of Investigation

The exploration method used in this work is a field survey based on the search and localization of outcrops with the help of the topographic map, and the global positioning system (GPS). At each sample point, outcrops were described, GPS coordinates registered, photographs taken and representative samples collected. The registered GPS readings were subsequently used to come out with a geologic map of the study area. Eight fresh rock samples of BIFs were collected and four thin sections were prepared at the Institute of Geological Research and Mining (IGRM) Laboratory in Yaoundé (Nkolbisong). The rocks were cut using a rock cutter in to rectangular cubes (4×2.5×1 cm) and placed on a glass slide using araldite gum. It is then polished until a thin section of 0.3 mm is reached. Detailed examination of thin sections were done using conventional techniques at the University of Buea. Mineral abbreviations recommendations by the IUGS Subcommission on the Systematics of Metamorphic Rocks are according to [71].

Whole rock geochemical analysis was realized on six representative samples of iron rich rock. Samples were submitted to Activation Laboratories (ACTLABS) in Canada for geochemical analysis following Total IDENT/4E-expl, analytic code 4E [72]. This package uses inductively coupled plasma (ICP) and instrumental neutron activation analysis (INAA) technologies to completely characterize geological samples. The major elements were analyzed by fusion-inductively coupled plasma (FUS-ICP) and they are expressed in percentage (%) of major oxides, with the detection limits varying from 0.005 to 0.1%. Loss of ignition (LOI) was determined by gravimetry (GRAV). Trace elements are analyzed by multiple techniques combining ICP and INAA analytical techniques. They are expressed in part per million (ppm), with the detection limits ranging from 0.1 to 20 ppm. Rare earth elements (REEs: La, Ce, Nd, Sm, Eu, Tb, Yb, Lu) are expressed in ppm. They were analyzed by INAA methods with the detection limits ranging from 0.05 to 5 ppm.

## IV. Results

### 4.1. Petrography

Banded iron formations (Fig. 2a) occur as blocks, flat stones and domes on the slope, valleys and on top of the crests of Nkol-Tsia hill in Gouap. They are light gray in colour and display fine to medium- grained. This rock type is strongly foliated characterized by: (i) alternating of light and dark bands. The dark bands are millimetric to decimetrric and mostly composed of magnetite. The light bands are millimetric to centimetric and compose of light minerals such as quartz; (ii) $S_1$ schistosity ($S_1$ foliation) generally oriented NNE-SSW and dipping 50º in the WNW. The Gouap BIFs display microband (millimeter to submillimeter) texture underlined by a concentration of magnetite minerals within the pervasive silica framework (Fig. 2a). Under the microscope the rock shows a granoblastic microstructure (Fig. 2b) made up of major mineral such as oriented magnetite (55 – 60%), mosaic and oriented quartz crystals (30 – 35%), and muscovite and limonite as accessory phase (2%). The main paragenesis of banded iron formations is Mgt + Qtz ± Ms ± Lm. This paragenesis characterizes the metamorphism under greenschist facies conditions. On the basis of their magnetic property, the Gouap BIFs are further subdivided into strongly magnetic BIFs, moderately magnetic BIFs and slightly magnetic BIFs (Fig. 2c, 2d). They have similar macroscopic and microscopic features.

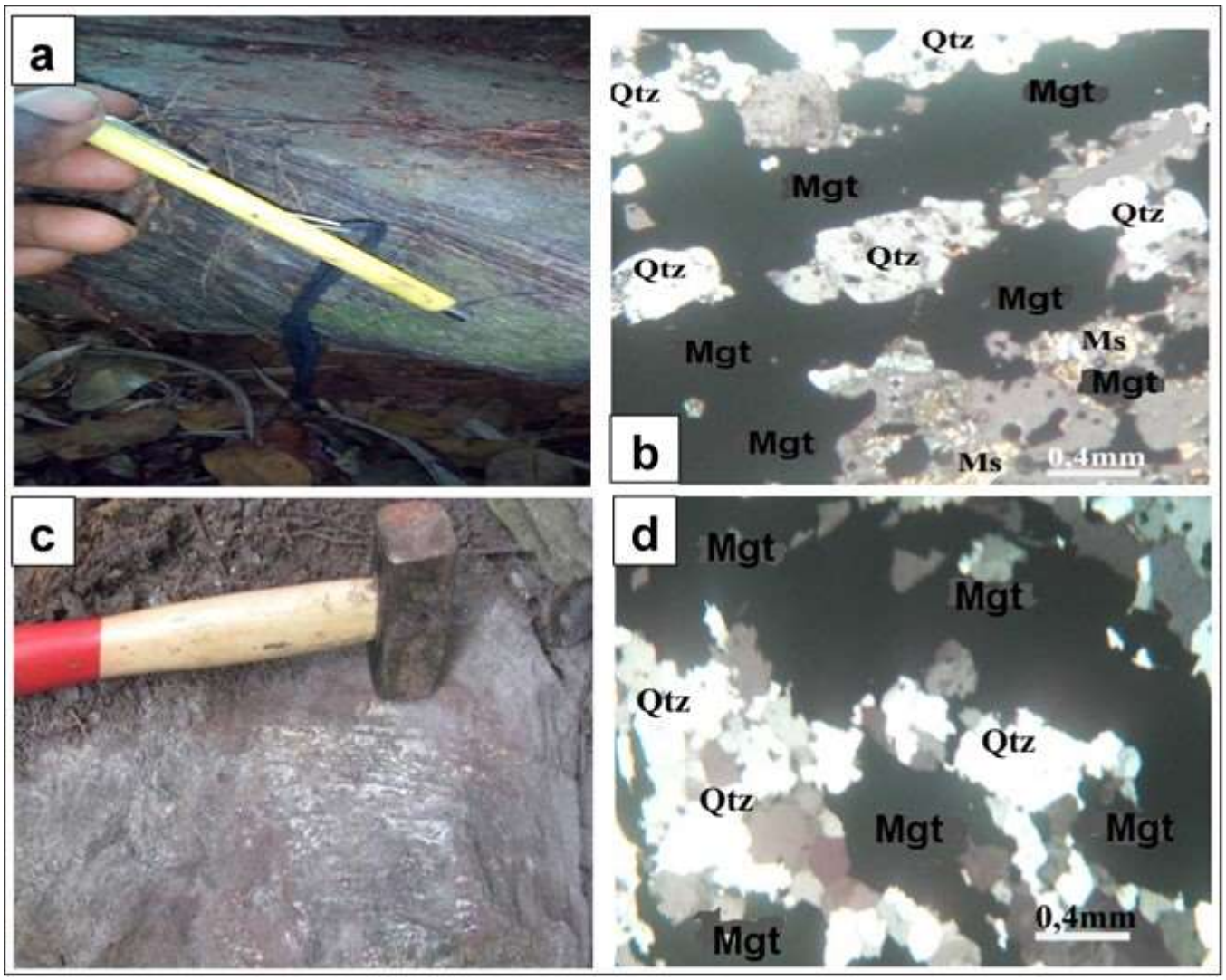


Figure 2. Field and laboratory photographs of Gouap BIFs. (a) Exposure of BIF displaying textural microband; (b) granoblastic microstructure showing the mineral composition; (c) exposure of slightly magnetic BIF; (d) Microscopic view of slightly magnetic BIF showing the mineral composition.

### 4.2. Geochemistry

The chemical composition of Gouap iron formations is presented in Table 1 below in term of major elements, trace elements and rare earth elements.

Table 1. Geochemical composition of Gouap iron deposits

| Analyte Symbol | Detection Limit | Analysis Method | Samples | | | | | |
|---|---|---|---|---|---|---|---|---|
| | | | GOP1 | GOP2 | GOP3 | GOP4 | GOP5 | GOP6 |
| $SiO_2$ (%) | 0.01 | FUS-ICP | 34.37 | 32.62 | 35.05 | 49.89 | 28.23 | 34.65 |
| $Al_2O_3$ | 0.01 | FUS-ICP | 0.23 | 0.22 | 0.23 | 0.2 | 0.41 | 0.34 |
| $Fe_2O_{3(T)}$ | 0.01 | FUS-ICP | 66.23 | 67.78 | 63.3 | 49.67 | 69.24 | 66.18 |
| MnO | 0.01 | FUS-ICP | 0.29 | 0.26 | 0.05 | 0.04 | 0.08 | 0.07 |
| MgO | 0.01 | FUS-ICP | 0.03 | 0.04 | 0.07 | 0.08 | 0.01 | 0.01 |

| | | | | | | | | |
|---|---|---|---|---|---|---|---|---|
| CaO | 0.01 | FUS-ICP | 0.14 | 0.05 | 0.05 | 0.06 | 0.05 | 0.08 |
| $Na_2O$ | 0.01 | FUS-ICP | < 0.01 | < 0.01 | < 0.01 | 0.01 | 0.01 | < 0.01 |
| $K_2O$ | 0.01 | FUS-ICP | < 0.01 | < 0.01 | < 0.01 | < 0.01 | < 0.01 | < 0.01 |
| $TiO_2$ | 0.005 | FUS-ICP | 0.006 | < 0.005 | 0.01 | 0.006 | 0.01 | 0.01 |
| $P_2O_5$ | 0.01 | FUS-ICP | 0.17 | 0.2 | 0.15 | 0.11 | 0.22 | 0.22 |
| $SO_3$ | 0.001 | TD-ICP | 0.006 | 0.006 | 0.003 | 0.003 | 0.016 | 0.011 |
| LOI | | GRAV | -0.86 | -0.61 | 0.38 | 0.38 | 0.66 | -0.74 |
| Total | 0.01 | FUS-ICP | 100.6 | 100.6 | 99.3 | 100.4 | 98.91 | 100.8 |
| $K_2O/Al_2O_3$ | | | 0,24 | 0,23 | 0,24 | 0,21 | 0,42 | 0,35 |
| $Al_2O_3/TiO_2$ | | | 38,33 | 44 | 23 | 33,33 | 41 | 34 |
| $SiO_2/Al_2O_3$ | | | 149,43 | 148,27 | 152,39 | 249,45 | 68,85 | 101,91 |
| Ag (ppm) | 0.5 | MULT INAA / TD-ICP | < 0.5 | < 0.5 | < 0.5 | < 0.5 | < 0.5 | < 0.5 |
| As | 2 | INAA | < 2 | < 2 | 2 | < 2 | 2 | < 2 |
| Au (ppb) | 5 | INAA | < 5 | < 5 | < 5 | < 5 | < 5 | < 5 |
| Ba | 3 | MULT INAA/FUSICP | 34 | 36 | 44 | 26 | 44 | 35 |
| Be | 1 | FUS-ICP | 1 | 1 | 2 | 2 | 1 | 1 |
| Bi | 2 | TD-ICP | 6 | 5 | 5 | 3 | 6 | 4 |
| Br | 1 | INAA | < 1 | < 1 | < 1 | < 1 | < 1 | < 1 |
| Cd | 0,5 | TD-ICP | 1.4 | 1.5 | 1.5 | 0.9 | 1.6 | 1.3 |
| Co | 1 | INAA | < 1 | < 1 | < 1 | < 1 | < 1 | < 1 |
| Cr | 1 | INAA | 10 | 7 | 8 | 9 | 13 | 17 |
| Cs | 0,5 | INAA | < 0.5 | 1 | < 0.5 | < 0.5 | < 0.5 | < 0.5 |
| Cu | 1 | TD-ICP | 8 | 9 | 8 | 6 | 9 | 8 |
| Hf | 0,5 | INAA | < 0.5 | < 0.5 | < 0.5 | < 0.5 | < 0.5 | < 0.5 |
| Hg | 1 | INAA | < 1 | < 1 | < 1 | < 1 | < 1 | < 1 |
| Ir | 5 | INAA | < 5 | < 5 | < 5 | < 5 | < 5 | < 5 |
| Mo | 2 | TD-ICP | < 2 | < 2 | < 2 | < 2 | < 2 | < 2 |
| Ni | 1 | TD-ICP | 3 | 5 | 4 | 4 | 5 | 4 |
| Pb | 5 | TD-ICP | 27 | 27 | 21 | 17 | 32 | 27 |
| Rb | 20 | INAA | < 20 | < 20 | < 20 | < 20 | < 20 | 30 |
| Sb | 0.2 | INAA | 0.3 | 0.2 | 0.4 | 0.2 | 0.2 | < 0.2 |
| Sc | 0.1 | INAA | 0.8 | 0.8 | 0.4 | 0.3 | 0.9 | 1.1 |
| Se | 3 | INAA | < 3 | < 3 | < 3 | < 3 | < 3 | < 3 |
| Sr | 2 | FUS-ICP | 6 | 4 | 3 | 3 | 2 | 3 |

Table 1. Continued

| | | | | | | | | |
|---|---|---|---|---|---|---|---|---|
| Ta | 1 | INAA | < 1 | < 1 | < 1 | < 1 | < 1 | < 1 |
| Th | 0.5 | INAA | < 0.5 | < 0.5 | < 0.5 | < 0.5 | < 0.5 | < 0.5 |
| U | 0.5 | INAA | < 0.5 | < 0.5 | < 0.5 | < 0.5 | < 0.5 | < 0.5 |
| V | 5 | FUS-ICP | < 5 | < 5 | < 5 | < 5 | < 5 | < 5 |
| W | 3 | INAA | < 3 | < 3 | < 3 | < 3 | < 3 | < 3 |

| | | | | | | | | |
|---|---|---|---|---|---|---|---|---|
| Y | 1 | FUS-ICP | 2 | 4 | 1 | 3 | 3 | 2 |
| Zn | 1 | TD-ICP | 17 | 15 | 14 | 12 | 17 | 15 |
| Zr | 2 | FUS-ICP | 14 | 19 | 8 | 20 | 6 | 11 |
| $Y/P_2O_5$ | | | 11.76 | 20 | 6.67 | 27.27 | 13.64 | 9.09 |
| La | 0.2 | INAA | 10.9 | 19.5 | 2.9 | 5 | 1.9 | 7.5 |
| Ce | 3 | INAA | 19 | 29 | 25 | 36 | 5 | 9 |
| Nd | 5 | INAA | 7 | 10 | < 5 | < 5 | < 5 | 5 |
| Sm | 0.1 | INAA | 0.7 | 1.3 | 0.3 | 0.5 | 0.3 | 0.9 |
| Eu | 0.1 | INAA | 0.2 | 0.3 | 0.1 | 0.2 | 0.2 | 0.2 |
| Tb | 0.5 | INAA | < 0.5 | < 0.5 | < 0.5 | < 0.5 | < 0.5 | < 0.5 |
| Yb | 0.1 | INAA | 0.5 | 0.5 | 0.5 | 0.5 | 0.6 | 0.5 |
| Lu | 0.05 | INAA | 0.1 | 0.14 | 0.16 | 0.11 | 0.11 | 0.14 |
| Mass (g) | | INAA | 2.64 | 2.707 | 2.515 | 2.141 | 2.645 | 2.67 |
| ΣREE | | | 38.9 | 61.24 | 34.46 | 47.81 | 13.61 | 23.74 |
| (La/Yb)N | | | 1.606 | 2.874 | 0.427 | 0.737 | 0.233 | 1.105 |
| (Ce/Sm)N | | | 1.9 | 1.5615 | 5.8333 | 5.04 | 1.167 | 0.7 |
| (Tb/Yb)N | | | 3.636 | 3.636 | 3.636 | 3.636 | 3.030 | 3.636 |
| Eu/Eu* | | | 0.610 | 0.737 | 0.363 | 0.663 | 0.727 | 0.565 |
| Ce/Ce* | | | -0.023 | -0.043 | 0.457 | 0.497 | -0.151 | -0.193 |

#### 4.2.1. Major elements

Major elements data for the representative samples from the Gouap banded iron formation are reported in Table 1. The analyses show very high $Fe_2O_{3(T)}$- enrichment (43.67 to 69.24 wt %; average = 63.73 wt %) compared to $SiO_2$ contents that vary between 28.23 to 49.89 wt. % with an average of 35.80 wt. %) suggesting that $Fe_2O_3$ and $SiO_2$ are the dominant components. These two major oxides are the most important components in the Gouap iron deposit, they represent 99.43% of the total bulk rock composition while the other major elements represent only 0.57%. This observation is supported with the petrographic studies where quartz and magnetite were the major minerals observed in the samples. Therefore, the major elements chemistry of these iron formations is remarkably with the main constituents being $Fe_2O_3$ and $SiO_2$. The high silica contents are attributed to the high metachert or quartz constituents of the iron formation. The alkali contents ($Na_2O + K_2O$ = 0.02%) are very low reflecting the rarity of silicate minerals in the iron deposit.

In the Pearson'correlation matrix (Table. 2) and Harker graphs (Fig. 3), $Fe_2O_{3(T)}$ shows positive correlation with $Al_2O_3$ ($R^2$ = 0.61), $P_2O_5$ ($R^2$ = 0.88) and $SO_3$ ($R^2$ = 0.61). An antithetic relationship (Table. 2) exists between $Fe_2O_{3(T)}$ and $SiO_2$ ($R^2$ = -0.98), $Fe_2O_{3(T)}$ and MgO ($R^2$ = -0.79) which is reflected in the very strong negative correlation (Fig. 3) between the two components and in the empirical inverse distribution of $SiO_2$ and MgO (0.01 to 0.08 wt. %) in the Fe-formation. The very strong negative correlation between $Fe_2O_{3(T)}$ and $SiO_2$ ($R^2$ = -0.98, Table 1, 2) suggests the incorporation of $Fe_2O_3$ and $SiO_2$ in different mineral phases. The very low $Al_2O_3$ (0.2 to 0.41%) contents indicate minor clastic dilution of the original chemical precipitates. The presence of $Al_2O_3$ and $TiO_2$ (0.005 - 0.01%) suggests trace inputs of detrital material. $Al_2O_3$ shows a strong positive correlation with $TiO_2$ ($R^2$ = 0.71) and a very strong positive correlation with $SO_3$ ($R^2$ = 0.97; Table. 2). The strong positive correlation between Al2O3 and TiO2 ($R^2$ = 0.71) shows that both probably originated from a common source [73]. Like Al, Ti is considered as an immobile element [74]. A positive correlation between $Al_2O_3$ and $TiO_2$ has also been reported from different BIFs in the world: in the BIF of Isua Supracrustal belt, west Greenland [75], in the BIF from the Bababudan Schist Belt, India [76], and in the Brockman iron-formation of the Dales Gorge Member, Western Australia [73]. The low contents of MnO (0.04 to 0.29 wt. %) and CaO (0.05 - 0.14 wt. %) combined with the low LOI (-0.86 - 0.66 %) indicates lack of carbonate and silicate minerals. The positive correlations between the other oxides show that, all these elements are associated to the same mineral phases.

Compared with the data from [77, 78], the bulk chemical composition of Gouap BIF in oxides is in the range of most

Archaean and Proterozoic iron-formations (Fig. 4a). The samples consist essentially of $Fe_2O_3$ which ranges from 43.67 to 69.24 wt % with a mean composition of 63.73 wt %. It has exceptionally high content in $Fe_2O_3$ compared to other BIFs. The mean contents of $TiO_2$, MnO, MgO, CaO, $Na_2O$, $K_2O$, $P_2O_5$ and $Al_2O_3$ in the Gouap BIFs are similar to those of the Lake Superior- type BIFs and the Algoma- type BIFs (Fig. 4a).

Table 2. Pearson's correlation matrix for Gouap iron prospect

| | SiO2 | Al2O3 | Fe2O3(T) | MnO | MgO | CaO | Na2O | K2O | TiO2 | P2O5 | SO3 | Co | Cr | Cu | Hg | Ba | Mo | Ni | Pb | Cd | Zn | Sb | La | Ce | Nd | Sm | Eu | Tb | Yb | Lu |
|---|---|---|---|---|---|---|---|---|---|---|---|---|---|---|---|---|---|---|---|---|---|---|---|---|---|---|---|---|---|---|
| SiO2 | 1 | | | | | | | | | | | | | | | | | | | | | | | | | | | | | |
| Al2O3 | -0,61 | 1 | | | | | | | | | | | | | | | | | | | | | | | | | | | | |
| Fe2O3(T) | -0,98 | 0,55 | 1 | | | | | | | | | | | | | | | | | | | | | | | | | | | |
| MnO | -0,34 | -0,31 | 0,45 | 1 | | | | | | | | | | | | | | | | | | | | | | | | | | |
| MgO | 0,75 | -0,80 | -0,79 | -0,26 | 1 | | | | | | | | | | | | | | | | | | | | | | | | | |
| CaO | -0,02 | -0,16 | 0,12 | 0,58 | -0,27 | 1 | | | | | | | | | | | | | | | | | | | | | | | | |
| Na2O | / | / | / | / | / | / | 1 | | | | | | | | | | | | | | | | | | | | | | | |
| K2O | / | / | / | / | / | / | / | 1 | | | | | | | | | | | | | | | | | | | | | | |
| TiO2 | -0,39 | 0,71 | 0,30 | -0,67 | -0,34 | -0,28 | / | / | 1 | | | | | | | | | | | | | | | | | | | | | |
| P2O5 | -0,85 | 0,76 | 0,88 | 0,22 | -0,93 | -0,02 | / | / | 0,38 | 1 | | | | | | | | | | | | | | | | | | | | |
| SO3 | -0,65 | 0,97 | 0,61 | -0,11 | -0,87 | -0,08 | / | / | 0,52 | 0,83 | 1 | | | | | | | | | | | | | | | | | | | |
| Co | / | / | / | / | / | / | / | / | / | / | / | 1 | | | | | | | | | | | | | | | | | | |
| Cr | -0,25 | 0,77 | 0,27 | -0,34 | -0,72 | 0,17 | / | / | 0,62 | 0,59 | 0,72 | / | 1 | | | | | | | | | | | | | | | | | |
| Cu | -0,97 | 0,50 | 0,96 | 0,42 | -0,68 | -0,10 | / | / | 0,23 | 0,84 | 0,57 | / | 0,10 | 1 | | | | | | | | | | | | | | | | |
| Hg | / | / | / | / | / | / | / | / | / | / | / | / | / | / | 1 | | | | | | | | | | | | | | | |
| Ba | -0,81 | 0,53 | 0,71 | -0,11 | -0,35 | -0,31 | / | / | 0,67 | 0,52 | 0,44 | / | 0,07 | 0,75 | / | 1 | | | | | | | | | | | | | | |
| Mo | / | / | / | / | / | / | / | / | / | / | / | / | / | / | / | / | 1 | | | | | | | | | | | | | |
| Ni | -0,34 | 0,41 | 0,26 | -0,19 | -0,18 | -0,84 | / | / | 0,13 | 0,44 | 0,44 | / | -0,05 | 0,49 | / | 0,37 | / | 1 | | | | | | | | | | | | |
| Pb | -0,89 | 0,75 | 0,90 | 0,39 | -0,93 | 0,15 | / | / | 0,25 | 0,92 | 0,85 | / | 0,45 | 0,86 | / | 0,54 | / | 0,34 | 1 | | | | | | | | | | | |
| Cd | -0,96 | 0,45 | 0,92 | 0,33 | -0,54 | -0,08 | / | / | 0,35 | 0,69 | 0,47 | / | 0,01 | 0,95 | / | 0,89 | / | 0,35 | 0,76 | 1 | | | | | | | | | | |
| Zn | -0,85 | 0,57 | 0,86 | 0,53 | -0,82 | 0,45 | / | / | 0,18 | 0,73 | 0,66 | / | 0,31 | 0,77 | / | 0,53 | / | 0,00 | 0,91 | 0,76 | 1 | | | | | | | | | |
| Sb | -0,10 | -0,36 | 0,05 | -0,01 | 0,40 | 0,17 | / | / | 0,25 | -0,36 | -0,49 | / | -0,39 | 0,00 | / | 0,44 | / | -0,48 | -0,29 | 0,29 | 0,00 | 1 | | | | | | | | |
| La | -0,14 | -0,43 | 0,27 | 0,81 | -0,11 | 0,19 | / | / | -0,74 | 0,21 | -0,23 | / | -0,35 | 0,32 | / | -0,29 | / | 0,10 | 0,17 | 0,12 | 0,12 | -0,26 | 1 | | | | | | | |
| Ce | 0,73 | -0,92 | -0,71 | 0,09 | 0,90 | -0,15 | / | / | -0,69 | -0,82 | -0,9 | / | -0,80 | -0,58 | / | -0,56 | / | -0,12 | -0,82 | -0,56 | -0,75 | 0,15 | 0,32 | 1 | | | | | | |
| Nd | -0,25 | -0,40 | 0,34 | 0,84 | -0,07 | 0,08 | / | / | -0,73 | 0,21 | -0,20 | / | -0,52 | 0,45 | / | -0,11 | / | 0,24 | 0,24 | 0,29 | 0,21 | -0,18 | 0,96 | 0,33 | 1 | | | | | |
| Sm | -0,11 | -0,26 | 0,27 | 0,63 | -0,24 | 0,12 | / | / | -0,57 | 0,35 | -0,09 | / | -0,06 | 0,28 | / | -0,34 | / | 0,16 | 0,20 | 0,03 | 0,05 | -0,43 | 0,94 | 0,18 | 0,82 | 1 | | | | |
| Eu | -0,10 | -0,04 | 0,20 | 0,59 | -0,32 | 0,00 | / | / | -0,66 | 0,36 | 0,19 | / | -0,08 | 0,29 | / | -0,37 | / | 0,42 | 0,36 | 0,00 | 0,17 | -0,76 | 0,80 | 0,11 | 0,77 | 0,81 | 1 | | | |
| Tb | / | / | / | / | / | / | / | / | / | / | / | / | / | / | / | / | / | / | / | / | / | / | / | / | / | / | / | 1 | | |
| Yb | -0,50 | 0,81 | 0,38 | -0,23 | -0,50 | -0,30 | / | / | 0,44 | 0,47 | 0,82 | / | 0,31 | 0,45 | / | 0,54 | / | 0,54 | 0,63 | 0,46 | 0,52 | -0,29 | -0,45 | -0,64 | -0,28 | -0,46 | 0,00 | / | 1 | |
| Lu | -0,18 | -0,12 | 0,18 | -0,28 | 0,20 | -0,52 | / | / | 0,38 | 0,11 | -0,25 | / | -0,11 | 0,23 | / | 0,43 | / | 0,27 | -0,19 | 0,28 | -0,32 | 0,41 | 0,07 | 0,11 | 0,06 | 0,16 | -0,27 | / | -0,35 | 1 |

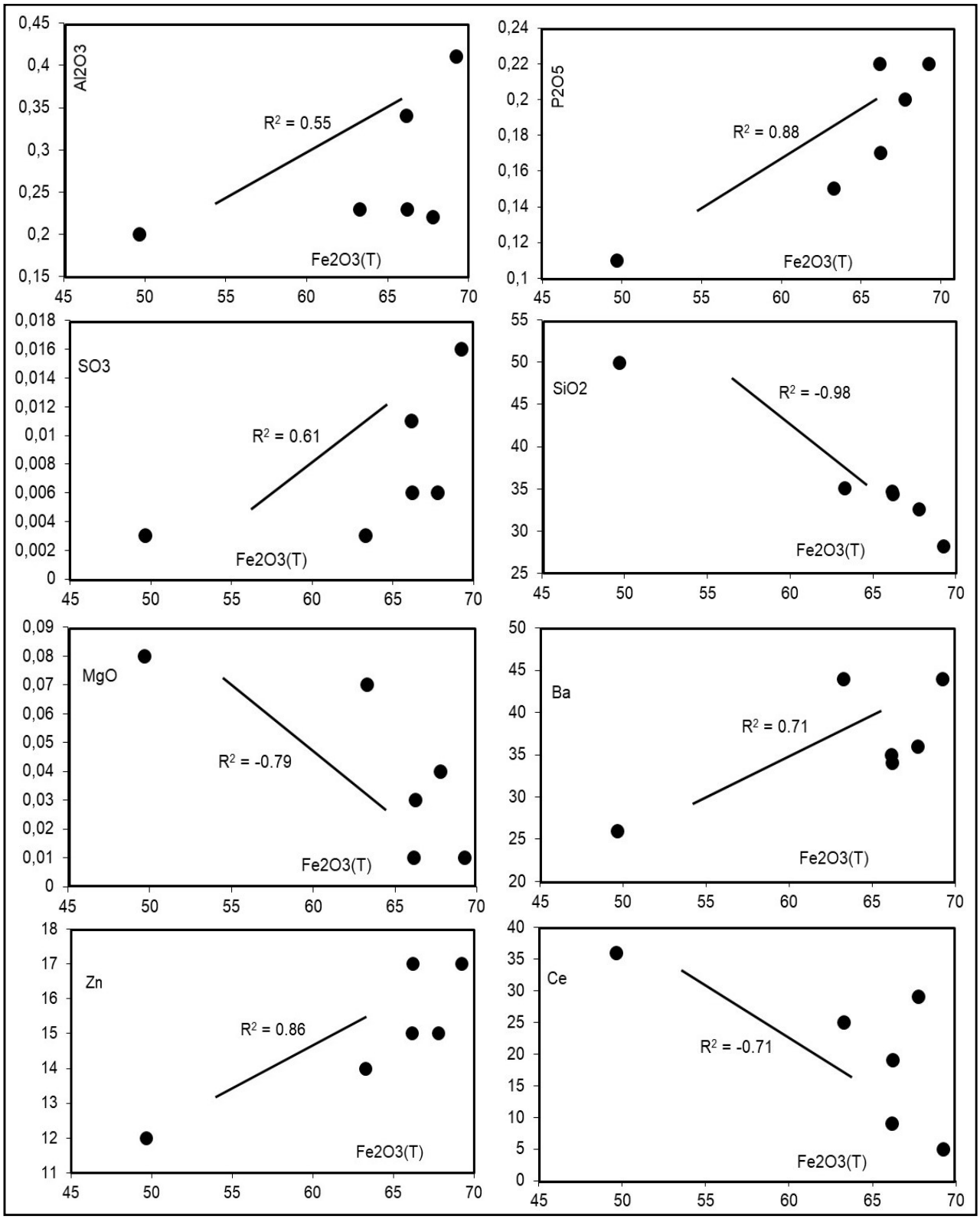


Figure 3. Selected Harker diagrams for major, trace and rare earth elements.

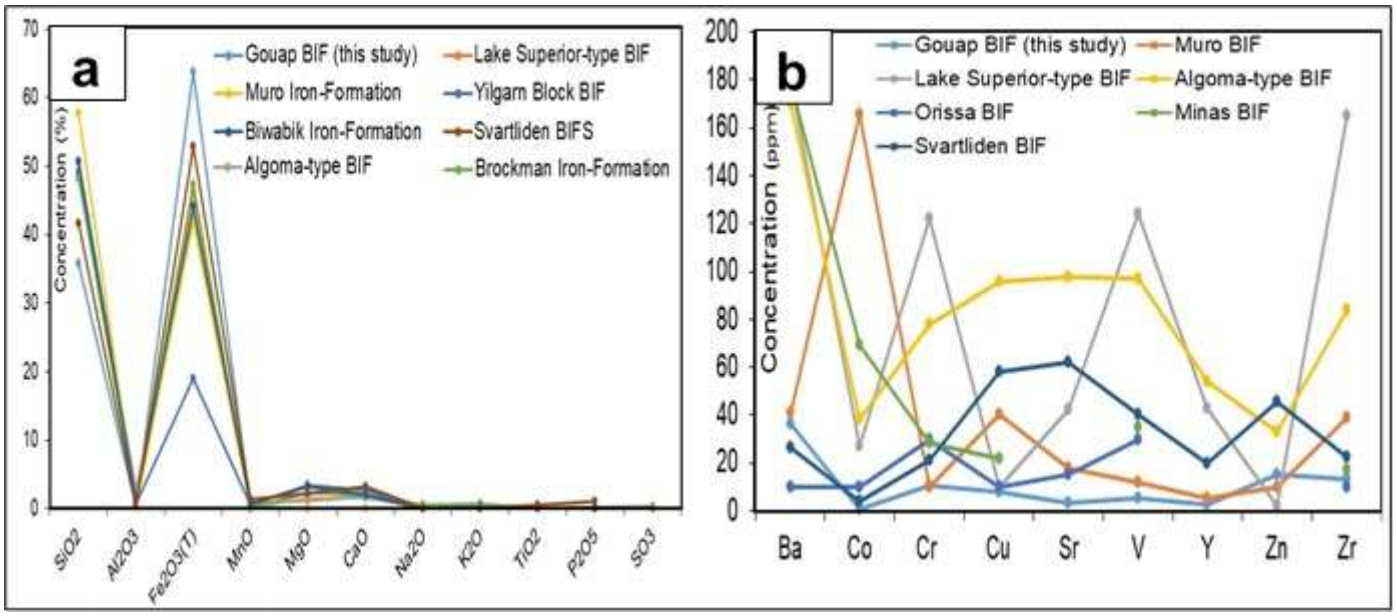


Figure 4. (a) Spidergram comparing the average major element composition of Gouap BIF with those of Lake Superior-type, Algoma-type, Yilgan Block, Biwabik, Muro [79], Brockman and Svartliden [80] BIFs; (b) Spidergram comparing the trace element composition of Gouap BIF and those of Lake Superior- type, Algoma- type, Muro, Orissa, Minas and Svartliden BIFs.

#### 4.2.2. Trace elements

The distribution of trace elements in the bulk samples are shown in Table 1 and no significant enrichments were observed. The contents of large ion lithophile elements (LILE) such as Ba (26 to 44 ppm), Rb (≤ 30 ppm) and Sr (2 to 6 ppm) are relatively elevated, while high field strength elements (HFSE) show depletion in Sc (0.3 – 1.1 ppm) and Y (1 - 4 ppm; Table 1). The concentration of the transition metals such as Cr (7 – 17 ppm), Cu (6 – 9 ppm), Ni (3– 5 ppm), Pb (17 – 32), V (<5 ppm) and Zn (12 – 17 ppm) are relatively noticeable. They are commonly used as indicators of direct volcanogenic hydrothermal input in chemical precipitates. In Table 2, $Fe_2O_{3(T)}$ displays mostly positive trends with trace elements. This tendency is reported in the binary plots (Fig. 4) where $Fe_2O_{3(T)}$ correlates positively with Cu ($R^2 = 0.96$), Ba ($R^2 = 0.71$), Pb ($R^2 = 0.90$), Cd ($R^2 = 0.92$) and Zn ($R^2 = 0.86$).

In general, the level of trace element concentrations in the Gouap BIFs is less than those of Lake Superior- type, Algoma- type, Muro, Minas, Orissa and Svartliden BIFs (Fig. 4b). These differences in the trace element concentrations may be attributed to the level of detrital material (clay constituents) in the original iron-formation. The $Al_2O_3$ content, which is a measure of the detrital dilution of iron-formations [81] is less in the Gouap BIF (0.27%) than in the Lake Superior- type (1.45%) and Algoma- type (3.06%) BIFs. The geochemistry of the various trace elements is summarized in Figure 4b.

#### 4.2.3. Rare earth elements

Rare earth element data from the Gouap BIF is presented in the Table 1. The REE distribution patterns and the variation observed in total REE contents range from moderate to high abundances (ΣREE = 13.61 to 61.24 ppm) with an average of 36.63 ppm. This relative elevated ΣREE (36.63 ppm) may be the consequence of addition of terrigenous debris to the chemical precipitate [76, 82]. A heavy covariance between $Fe_2O_{3(T)}$ and Ce is observed with a coefficient of correlation of -0.71 (Table 2 and Fig. 3). The following relations: $Eu/Eu^* = Eu_N/(0.67Sm_N + 0.33Tb_N)$ according to [83] and $Ce/Ce^* = \log[Ce_N/(La_N*Nd_N)^{1/2}]$ after [84] are used to calculate Eu and Ce anomalies values respectively. REE patterns (Fig. 5) are fractionated ($La_N/Yb_N$ = 0.23-2.88) with relative light rare earth elements (LREEs; $Ce_N/Sm_N = 0.7 – 5.83$) depletion and relative heavy rare earth elements (HREEs) enrichment ($Tb_N/Yb_N = 3.03 – 3.64$). They show a weak negative Eu anomaly (Eu/Eu* = 0.36 – 0.73) and a slightly positive Ce anomaly (Ce/Ce* = -0.19 – 0.5).

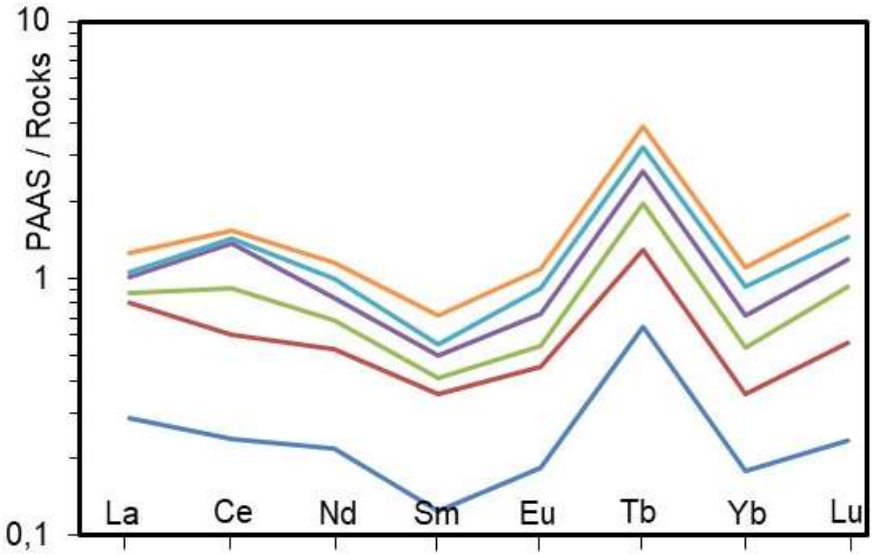


Figure 5. PAAS normalized rare earth elements pattern for the Gouap BIFs. Normalization values are according to [85].

## V. Discussion

### 5.1. Iron bearing rocks of Gouap

The Gouap area is found in the southern part of Cameroon and belongs to the Nyong series situated NW corner of the Ntem complex. The iron bearing rocks recorded in the Gouap area are banded iron formations (BIFs), they are subdivided into strongly, moderately and slightly magnetic and have the same petrographic features. They show microband texture and granoblastic microstructure. The mineral assemblage indicates that they undergone the metamorphism of greenschist facies conditions. Banded iron formations are well known within the Precambrian Ntem complex in southern Cameroon (e.g. [37, 38 - 56, 86, 87]). They are intercalated with metasandstones and metasiltstones [40].

### 5.2. The most diagnostic fingerprints of the source metals from Gouap

The bulk chemical composition of Gouap BIFs is in the range of most Archaean and Proterozoic iron-formations. The trend (Fig. 6a) of the Gouap BIF is closer to the Svartliden and Orissa one for Co, Cr, Ni and Cu (6 – 9 ppm) contents. The average on composition for V and Zn are too far from both types. It is not possible to conclude about Pb and Sc because they are not represented in most of the various iron formations. The most diagnostic fingerprints of the source metals during chemical precipitation are the ferromagnesian trace elements such as Ni, Cr and Co [75, 88, 89]). According to Figure 6a, the Gouap iron deposit contains 4.17 ppm of Ni in average, ranged between 3 and 5 ppm. The Cr values range between 7 and 17 ppm with an average of 10.67 ppm. The Co (<1 ppm) content is under detection limit (1 ppm) and the detection limit is high to quantify it properly. So, it is not possible to conclude about Co. Therefore, we suggest that the most diagnostic fingerprints of the source metals of Gouap are probably Ni, Cr and Cu. When the sum of Co + Cu + Ni is plotted against the sum of REE (Fig. 6b), it presents a horizontal trend with almost constant sum of metals and variation in ΣREE values. All the points are plotted close to the hydrothermal deposits field. This field represents data from green muds and/or nontronite and is concluded to be the result of mixing of hydrothermal solutions from sub-oceanic basalts with ocean water [90]. The horizontal trend of the Gouap BIF is due to Cu which tends to be mobile, particularly at high temperatures, whereas Co is considered immobile [91]. Even if Ni is normally also immobile [91], it tends to have been mobile in the Gouap BIF (Fig. 6b). Thus Co, Ni, and Cu are probably formed from a precipitation from a hydrothermal fluid.

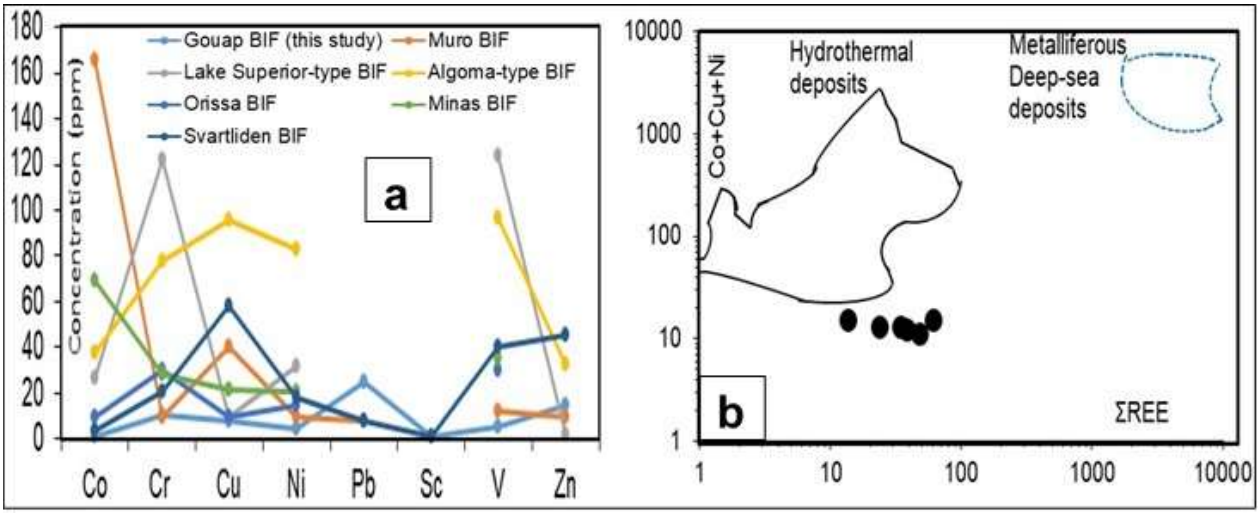


Figure 6. (a) Some metal contents in the Gouap BIF compared with those from classical Algoma- and Superior- type BIF trends, and Muro, Orissa and Svartliden BIFs; (b) Co + Ni + Cu vs. ΣREE after [75]). The area labelled hydrothermal deposits encloses data for deposits from the Famous and Galapagos regions, which are mostly green muds and/or nontronite, and the area labelled metalliferous deep-sea sediments represents mostly deep-sea drilling project samples from East Pacific sites [92].

### 5.3. Nature, Source of protoliths and depositional setting

Based on silica content (average = 35.80% $SiO_2$) compared to $Fe_2O_{3(T)}$ content (average = 63.43), the Gouap iron deposits fall into the group of oxide facies after [93, 94, 95], with magnetite as dominant mineral. This result is in accordance with the majority of iron deposit in Cameroon where either hematite or magnetite are dominant mineral. The oxide facies iron deposit is also recorded in Metzimevin [37], Nkout [41], Kpwa–Atog Boga [48] and Pout Njouma [56]. Meanwhile, the silicate facies is reported to the Njweng prospect [43], Elom [46], Mafé [57] and Messondo iron deposit [51].

Due to the changeability of the $K_2O/Al_2O_3$ values in clays (< 0.3) and in alkali feldspars (0.3–1), [96] proposed the use of $K_2O/Al_2O_3$ ratio in order to discriminate the contribution of alkali feldspars to the parent rock of pelitic sediments. Therefore, the $K_2O/Al_2O_3$ values of the Gouap metasediments ranging from 0.21 to 0.42 (mean: 0.28) indicate a minimal involvement of alkali feldspars to the parent rock, implying that their composition is not entirely felsic. The $Al_2O_3/TiO_2$ ratio has been proven to specify the source of sedimentary rocks. Indeed, the $Al_2O_3/TiO_2$ ratio less than 14 is a characteristic of mafic precursors, whereas the $Al_2O_3/TiO_2$ ratio ranging between 19 and 28 characterizes sediments derived from intermediate igneous rocks [97]. The $Al_2O_3/TiO_2$ ratio of the Gouap iron prospect varies between 23 and 44 (average: 35.61), which implies that these rocks originated mainly from a felsic igneous parent source. The Gouap iron occurrence also displays some light terrigenous input in its geochemistry. The very low content in Al2O3 (average: 0.27 wt.%) and Zr (less than 20 ppm, except for sample GPO4: Zr = 20 ppm), both being immobile elements [74], proves that the detrital input was low in the Gouap iron formations [3]. These very low contents in Al2O3 and Zr support the fact that Gouap iron formation belongs to the Algoma- type. Very low Al2O3 contents indicate that iron formations were deposited in an environment devoid of siliciclastic detrital input in opposition to deep-shelf limestones that have distinctly greater Al2O3 contents [15].

The provenance of the parent rock of the Gouap BIF can be inferred using the discrimination diagram $\log(Fe_2O_{3T}/K_2O)$ vs. $\log(SiO_2/ Al_2O_3)$ adapted from [98]. According to this diagram (Fig. 7a), the majority of samples (samples GOP1, GOP2, GOP3, GOP4) fall into the field of quartz arenite and 2 samples (samples GOP5, GOP6) have plotted in the field of Fe- sand. Thus the Gouap BIFs have the composition of quartz arenite and Fe- sand. Therefore, we suggest that the protoliths of Gouap iron formations include quartz arenite and Fe- sand. This is a new result for the BIFs in Cameroon. It differs with the Messondo [51] and Pout Njouma BIFs [56] that derived from Fe- sand, it also different with Kpwa-Atog Boga [48] and Bipindi iron bearing rocks [53] that have Fe- shale and shale as protoliths. Floyd et al. (1989) proposed the use of Sr vs. Ba diagram to constrain the source characteristics of metasediments considering that Sr and Ba are relatively immobile during metamorphism. Plotted in this diagram, all the studied rock samples cluster to

the field of mature sediments (Fig. 7b), suggesting that the Gouap iron bearing rocks derived from mature quartz arenite and Fe-sand (Fig. 7a). The Precambrian age (Fig. 7c) of Gouap iron deposits has inferred from a ternary diagram $Al_2O_3$ - $SiO_2$ - $Fe_2O_{3(T)}$ according to [100]. Similar result is observed in Messondo [51] and Pout Njouma iron formations [56], and comforts with the post Archean age obtained in Kpwa-Atog Boga [48]. The Precambrian age for the Gouap iron mineralization is also conform with the geochemical data that show low $Al_2O_3$, $TiO_2$, $P_2O_5$, CaO and MgO contents relative to post-Precambrian deposits [100, 101].

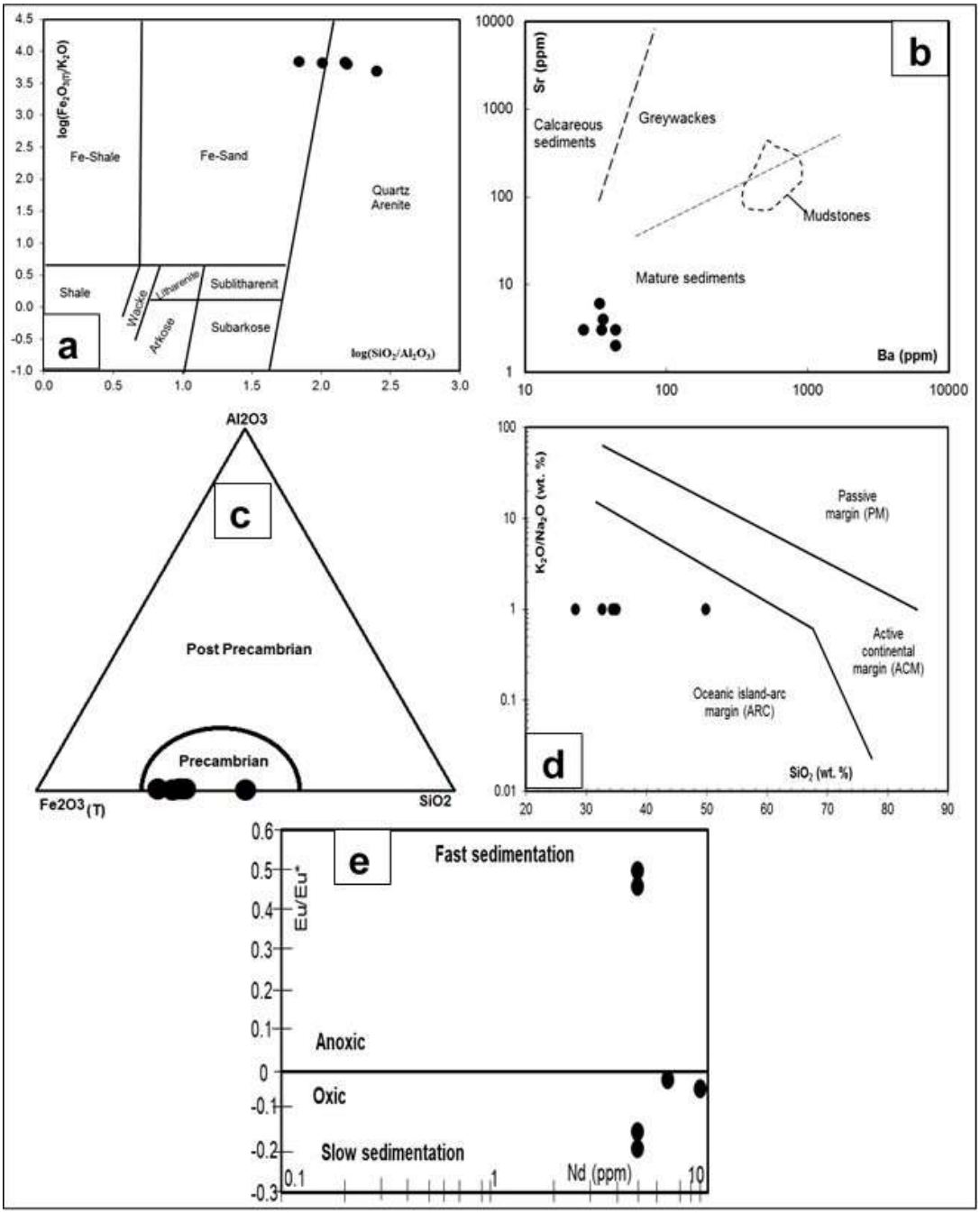


Figure 7. (a) Discriminative log ($Fe_2O_{3(T)}/K_2O$) vs. log ($SiO_2/Al_2O_3$) plot [98]showing the chemical composition of Gouap iron deposits; (b) Position of Gouap iron samples in Sr vs. Ba diagram after [99]; (c) $Al_2O_3$-$SiO_2$-$Fe_2O_3$ triangular diagram after [100]showing the plot of Gouap iron rocks samples in the Precambrian field; (d) $K_2O/Na_2O$ vs. $SiO_2$ diagram according to [102]

for discriminating the tectonic settings of the Gouap iron deposit. ARC (oceanic island-arc margin), ARM (active continental margin), and PM (passive margin); (e) Position of Gouap iron- bearing rocks in the Ce/Ce* vs. Nd graph after [103].

Regarding at the $K_2O/Na_2O$ vs. $SiO_2$ diagram after [102] discriminating the tectonic settings (Fig. 7d), all the samples cluster into the field of Oceanic Island-arc Margin (ARC). This result is similar to the Messondo [51] and Pout Njouma [56] iron formations, but in contrast the Kpwa-Atog Boga metasediments [48] is deposited in an Active Continental Margin. It also contrasts with the Ntem metasediments deposited in the Passive Margin (PM) or between the PM and ACM [53]. However, some metasedimentary rocks have been deposited in a continental environment within the Nyong unit [62]. During the protolith emplacement, there was abundant contribution of continental sediments at the boundary of a shallow basin [86].

The Ce anomaly (Ce/Ce* = -0.19-0.52) is calculated to investigate for the conditions of the formation of the studied iron deposits. The values are plotted on the Ce/Ce* vs. Nd concentrations as from the diagram of [103]. The graphical representation shows that most of the investigated samples fall into the oxic field with slow sedimentation (Fig. 7e) except samples GOP3 and GOP4 that fall within the anoxic domain and fast sedimentation. Therefore, we suggest that the Gouap iron formation were deposited under oxic conditions with slow sedimentation accompanied with minor input of anoxic conditions where sedimentation was fast. This new result for de iron deposits in Cameroon differs with the ones obtained for the Messondo [51] and Pout Njouma BIFs [56] deposited under anoxic conditions and fast sedimentation.

### 5.4. Origin of chemical components in the Gouap BIFs: source of Fe and silica

Different models have been suggested to clarify the origin of iron and silica in BIFs. BIFs may be derived either from (i) the hydrothermal alteration of oceanic crust, from continental sources (e.g., [2, 104, 105]), or from (ii) a mixture of seawater hydrothermal fluids and weathering of continental crustal material [32, 106]. Based on the mineralogical variations, chemical and isotopic compositions, different approaches have been suggested to distinguish between the aforementioned origins. The chemical composition of the Gouap iron formations indicates that the major components are $Fe_2O_3$ and $SiO_2$, followed by lesser concentrations of $Al_2O_3$, $TiO_2$, MnO, MgO and CaO (Table 1). High contents of $Fe_2O_3$ and $SiO_2$ in the studied rocks indicate the purity of the chemical precipitates. This is in accordance with [107] who reported that iron and silica are the principal constituents of BIFs derivate from seawater.

According to [108], hydrothermal metal- rich deposits could be distinguished from hydrogenous deposits formed by diagenetic processes on the basis of the relative abundance of $SiO_2$ and $Al_2O_3$. The Si/Al ratio is commonly used to detect eventual hydrogenous, respectively hydrothermal material supply. It is worth underlining here that the Si/Al ratio has been used to distinguish between hydrothermal Fe–Mn crusts, rich in Si and characterized by a Si/Al ratio >5.1, and hydrogeneous Fe-deposits (nodules), whose typical Si/Al ratio is 3, the same as marine sediments [109]. The average Si/Al ratio of the studied iron formation is averagely 145.05 pointing towards the hydrothermal origin of the studied iron formation. Therefore, the plot of the studied rock samples in the diagram $TiO_2$ vs. $Al_2O_3$ of [108] fall within the hydrothermal field (Fig. 8a), this is in accordance with the result of [110] indicating that pure hydrothermal deposits contain very little Al and have high Al/Ti ratios. The Fe and Mn serve as partial hydrothermal proxies, while $Al_2O_3$ and $TiO_2$ are usually used as tracers for clastic input [3, 111]. The hydrothermal origin for iron formations is largely reported in the Ntem Complex (e.g. [42, 45 - 48, 50, 54). Suh et al. (2008) suggested that the Metzimevin iron deposit is the result of hypogene leaching of gangue minerals from, and further hematitization of, an itabirite protore.

Contamination of hydrothermal deposits by pelagic and terrigenous deep-sea sediments enriches them in components such as Ti and Al, resulting drastic lowering of the Fe/Ti ratios and increase in the Al/(Al + Fe + Mn) ratio. Base on the Fe/Ti vs. Al/(Al + Fe + Mn) diagram (Fig. 8b) of [112], all of the studied samples cluster on the Red Sea hydrothermal deposits (RS). RS origin of BIFs is also reported in Elom [46], while East Pacific Rise hydrothermal deposits (EPR) have been recorded in Messondo [51], Kelle Bidjoka [52] and Pout Njouma [56]. EPR and RS origin was proposed for Zambi BIFs [45], Meyomessi [42] and Kpwa-Atog Boga BIFs [50].

Hydrothermal fluids have been established by [113] as the source that induces a positive Eu anomaly in BIFs, while [114] indicated that the seafloor hydrothermal fluid shows positive Eu anomaly. Strong positive Eu anomalies signify hydrothermal fluids of high-temperature (> 250 °C), while weak to no Eu anomaly indicates fluids of low-temperature

(< 200°C [3]). It is possible that the slightly low negative Eu anomalies of the Gouap iron- rich rocks are inherited from low- temperature hydrothermal fluids. Moreover, the fraction of seawater and hydrothermal fluids can be assessed using the Sm/Yb vs. Eu/Sm diagram of [115]. Plotted on this diagram (Fig. 8c), the Gouap BIFs plot near Low- temperature hydrothermal fluids (< 0.1%) and Seawater fields, and far away from high-temperature hydrothermal fluids. This indicates that mixing of seawater and less amount (< 0.1%) of low-temperature hydrothermal fluids (< 200 °C) might have occurred during the deposition of the studied iron formations. This is in accordance with the result of [48] and contrasts with the one of [56] that shows the contribution of Seawater. In the work of [52] magnetite pyroxene gneiss and pyroxene BIFs show high- T hydrothermal fluid contribution while grunerite BIFs and garnet- bearing magnetite pyroxene gneiss are devoid of hydrothermal input and plot close to hydrogenetic Fe-Mn crust field. A predominantly hydrothermal origin is also consistent with relatively low $Y/P_2O_5$ ratios (average: 14.74), similar to the ratios expected in pure hydrothermal deposits [110]. This is confirmed by the $Y/P_2O_5$ versus Zr/Cr discrimination diagram [110] where the studied samples plot very close to the hydrothermal sediment field (Fig. 8d).

We used the Sm/Yb and Eu/Sm ratios to quantify the Eu anomaly and evaluate the amount of hydrothermal fluids and seawater in the source [115, 116]. The Sm/Yb ratio is particularly sensitive to the presence of high-pressure residual metamorphic phases [116]. In the Sm/Yb - Eu/Sm graph proposed by [116], three of the samples (samples GOP3, GOP4 and GOP5) in this study fall on the mixing line (Fig. 86). Their sample position (Fig. 8e) suggests a high-temperature hydrothermal fluid input of 1–5%. The other three samples (samples GOP1, GOP2 and GOP6) fall away. This mixing diagram may provide an indication of the locus of the depositional site relative to the hydrothermal source vent: when the depositional site is near the hydrothermal source vent, samples will be qualitatively closer to the high-temperature hydrothermal fluid end-member whereas when the depositional site is more distal, the samples will be qualitatively closer to the seawater end-member [116]. In this study, three samples (samples GOP3, GOP4 and GOP5) have values that reflect between 1 to 5% of a high-temperature hydrothermal fluid input, this suggests that the Gouap iron formations was deposited close to the distal position.

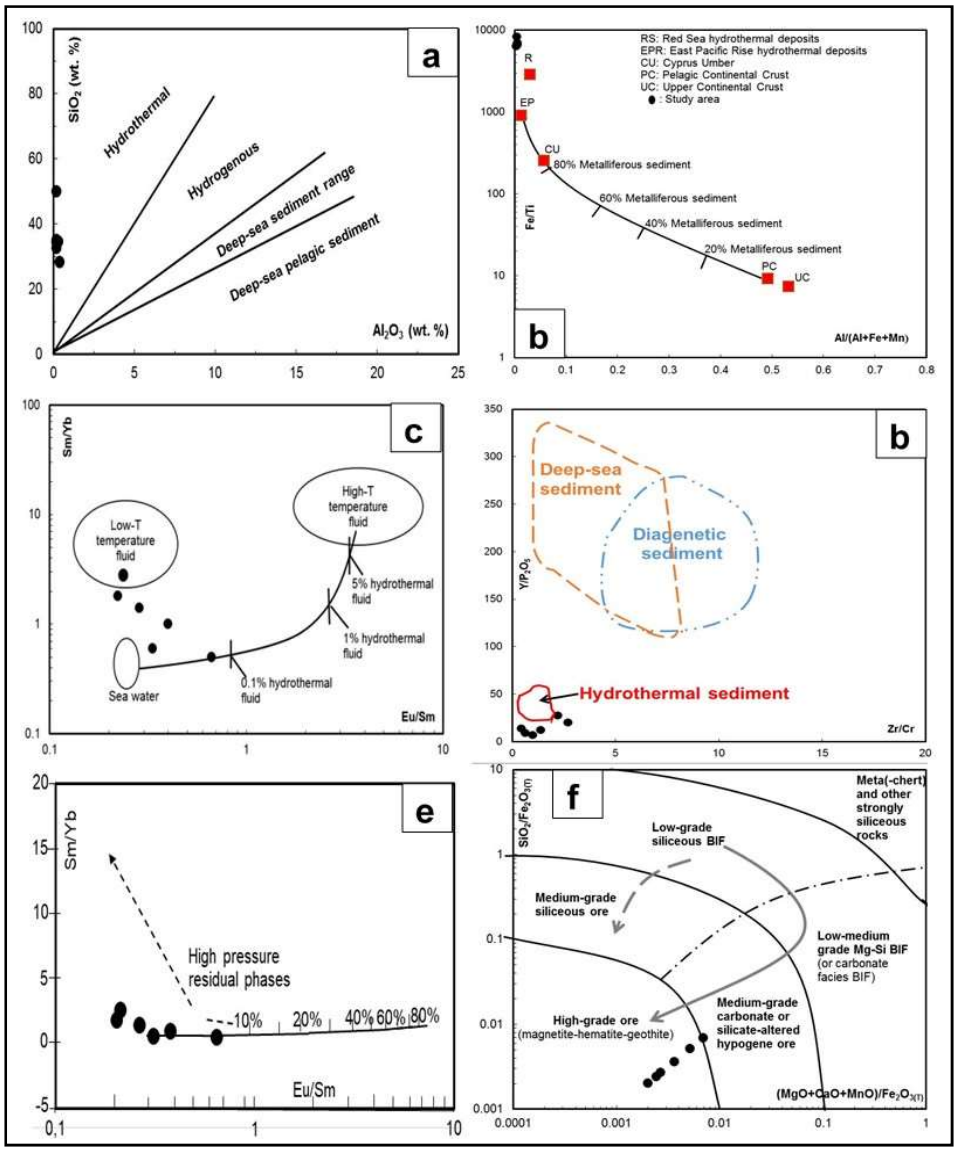


Figure 8. Discrimination diagrams of: (a) $SiO_2$ vs. $Al_2O_3$ indicating the hydrothermal affinity of the studied iron formations; (b) Fe/Ti versus Al/(Al + Fe + Mn) diagram of Gouap iron-formation. The curve represents mixing of East Pacific Rise deposits (EPR) with pelagic sediments (PC) whereas the numbers indicate the approximate percentage of EPR in the mixture (adopted from [112].

lso indicated are compositions for mean upper continental crust (UC [85]), Red Sea hydrothermal deposits (RS [110]) and the Cyprus umber (CU), (c) plot of Sm/Yb vs. Eu/Sm for the Gouap BIFs modified after Alexander et al. (2008); (d) $Y/P_2O_5$ versus Zr/Cr binary discrimination diagram [110] indicating the hydrothermal origin of the studied samples; (e) Graph of Eu/Sm – Sm/Yb ratios for the Gouap iron samples assessing the high- T hydrothermal fluids potential influence on the iron formations via a mixing line [116]. High-T hydrothermal fluids and seawater data are from [117, 118] respectively; (f) Whole-rock (MgO + CaO + MnO)/$Fe_2O_3$ total versus $SiO_2/Fe_2O_3$ total discrimination diagram [119] depicting the medium- to high-grade types of the Gouap iron deposit. Discrimination fields and arrows showing alteration trends, including MgO + CaO + MnO- rich (solid arrow) and –poor (dash arrow) stages.

### 5.5. Iron potential

The high concentration of $Fe_2O_{3(T)}$ in the Gouap iron deposits (averagely 63.73 wt%) shows that it has a very interesting potential for exploitation. [120] divided iron ores in three main categories based on the Fe percentage: (i) high grade iron ores with iron percentage > than 65%, (ii) average grade with iron ranging between 52 - 65% and (iii) low grade

with Fe < 52%. In China, the iron ore is classified as low grade (< 50% Fe) and high grade (> 50% Fe; [121]), whereas in Brazil, Canada, and Australia, high-grade iron ore types are characterized by >64% [35]. The $Fe_2O_{3(T)}$ contents (averagely 63.73 wt%) for the Gouap BIFs can be classified as high-grade [121] or medium-grade [120] iron ores by global standards.

The potential of iron ore mineralization is generally viewed not only by using the iron percentage, but also the deleterious elements encountered such as $P_2O_5$ and S [122]. The acceptable contents of phosphorous and sulphur in commercial ores should be lower than 0.07% P and 0.1% S respectively [122, 123]. The average P and S contents for the Gouap iron deposits are 0.18% and 0.01% respectively. Though that of $P_2O_5$ is slightly high, these BIFs still fall within the acceptable levels for commercial ores.

Angerer et al. (2012) has proposed the use of the bulk geochemical composition of iron ore to identify carbonate- or silicate- rich zones in BIF and illustrate the evolution of hypogene hydrothermal alteration zones through time. Angerer et al. (2012) proposed a discrimination plot for iron ore types based on major total oxide ratios $SiO_2/Fe_2O_3$ and $(MgO + CaO + MnO)/Fe_2O_3$. Higher (Mg + Ca + Mn)/Fe and lower Si/Fe ratios indicate carbonate–silicate metasomatism and the decrease in the Si/Fe and (Mg + Ca + Mn)/Fe ratios of the high- grade magnetite–hematite–goethite ores in all high-grade ore deposits worldwide. This diagram emphasizes the ratio between primarily dominant silica and elements added through carbonate–silicate alteration (mainly Mg, Ca, Mn) and therefore discriminates unaltered siliceous BIF from BIF that was likely hypogene-altered and associated hypogene ore. In this diagram, the Gouap mineralized iron samples plot within the field of high- grade siliceous ore (Fig. 8f), contrasting the result obtained by [50] in the same study area. This new result suggests that the Gouap iron deposits host high- grade siliceous ore with magnetite being the predominant mineral.

Petrographical and geochemical studies of banded iron formations were carried out in the Gouap area. The rocks were analyzed chemically by ICP-MS combined with INAA and the following conclusions are drawn:

1. The Gouap area is found in the southern part of Cameroon and belongs to the Nyong series situated NW corner of the Ntem complex. The Gouap BIFs show microband texture and granoblastic microstructure. The mineral assemblage indicates that they undergone the metamorphism of greenschist facies conditions.

2. The chemical composition of the Gouap iron formations shows that the major components (99.43%) that are $Fe_2O_3$ and $SiO_2$ indicate the purity of the chemical precipitates. The Gouap iron deposit fall into the group of oxide facies with magnetite as dominant mineral and the most diagnostic fingerprints of the source metals are probably Ni, Cr and Cu.

3. Large ion lithophile elements (LILE) are relatively elevated compared to high field strength elements (HFSE) and the concentration of some transition metals are relatively noticeable. The relative elevated of ΣREE (average = 36.63 ppm) may be the consequence of addition of terrigenous debris to the chemical precipitate.

4. The Gouap iron deposit shows a minimal involvement of alkali feldspars to the parent rock implying that their composition is not entirely felsic. The Gouap BIF also displays some light terrigenous input in its geochemistry implying that it belongs to the Algoma- type and indicates that the BIFs were deposited in an environment devoid of siliciclastic detrital input.

5. The Gouap iron formations derived from Precambrian mature quartz arenite and Fe-sand that were deposited in an Oceanic Island-arc Margin (ARC) setting under oxic conditions with slow sedimentation accompanied with minor input of anoxic conditions where sedimentation was fast. This constitutes a new result for de iron deposits in Cameroon.

6. The overall data and graphical representations pointing to hydrothermal origin and all of the studied samples cluster on the Red Sea hydrothermal deposits (RS). They exhibit Low-temperature hydrothermal fluids (< 0.1%) and Seawater, indicating that mixing of seawater and less amount (< 0.1%) of low-temperature hydrothermal fluids (< 200°C) might have occurred during their deposition. A half number of samples have values that reflect between 1 to 5% of a high-temperature hydrothermal fluid input suggesting that the Gouap iron formations were deposited close to the distal position.

7. The high concentration of $Fe_2O_{3(T)}$ in the Gouap iron deposit (average = 63.73 wt%) shows that it has a very interesting potential for exploitation and this iron contents can be classified as high- grade or medium- grade iron ores by global standards, and it fall within the acceptable levels for commercial ores. Gouap BIFs host high- grade siliceous ore with magnetite being the predominant mineral. This also constitutes a new result for the iron deposit in Cameroon.

## REFERENCES


[1] Klein, C. Some Precambrian banded-iron formation (BIFs) from around the world: their age, geologic setting, mineralogy, metamorphism, geochemistry and origin. Am. Miner. 2005; 90, 1473–1499.

[2] Bekker, A., Slack, J.F., Planavsky, N., Krapež, B., Hofmann, A., Konhauser, K.O., and Rouxel, O.J. Iron formation: The sedimentary product of a complex interplay among mantle, tectonic, oceanic, and biospheric processes: Economic Geology and the Bulletin of the Society of Economic Geologists. 2010; 105: 467–508, doi:10.2113/gsecongeo.105.3.467.

[3] Basta. F.F., Maurice. A.E. Fontboté. L. Favarger. P.Y. Petrography and geochemistry of the banded iron formation (BIF) of Wadi Karim and Um Anab. Eastern Desert. Egypt: Implications for the origin of Neoproterozoic BIF. Precambrian Research. 2011; 187: 277-292

[4] Klein, C. and Beukes, N.J. Time Distribution, Stratigraphy, and Sedimentlogical Setting, and Geochemistry of Precambrian Iron Formation. In: Schopf, J.W., Klein, C. (Eds.), the Proterozoic Biosphere: a Multidisciplinary Study. Cambridge University Press, New York. 1992; 139–146.

[5] Lowe, D.R., Tice, M.M. Tectonic controls on atmospheric, climatic, and biological evolution 3.5–2.4 Ga. Precambrain Res. 2007; 158: 177–197.

[6] Haugaard, R., Frei, R., Stendal, H., Konhauser, K. Petrology and geochemistry of the ~2.9 Ga Itilliarsuk banded iron formation and associated supracrustal rocks, West Greenland: source characteristics and depositional environment. Precambrian Res. 2013; 229: 150–176.

[7] Taylor, S.R., McLennan, S.M. The composition and evolution of the continental crust: rare earth element evidence from sedimentary rocks. Philos. Trans. R. Soc. Lond. 1981; 301: 381–399.

[8] Eriksson, P., Martins-Neto, M.A., Nelson, D.R., Aspler, L.B., Chiaranzelli, J.R., Catuneanu, O., Sakar, S., Altermann, W., Rautenbach, C.J. An introduction to Precambrian basins: their characteristics and genesis. Sediment. Geol. 2001; 141:142, 1–35.

[9] Barley, M., Bekker, A., Krapez, B. Late Archean to early paleoproterozoic global tectonics, environmental change and the rise of atmospheric oxygen. Earth Planet. Sci. Lett. 2005; 238: 156–171.

[10] Viehmann, S., Bau, M., Smith, A.J.B., Beukes, N.J., Dantas, E.L., and Bühn, B. The reliability of ~2.9 Ga old Witwatersrand banded iron formations (South Africa) as archives for Mesoarchean seawater: Evidence from REE and Nd isotope systematics: Journal of African Earth Sciences. 2015; 111: 322–334, doi:10.1016/j.jafrearsci.2015.08.013.

[11] Konhauser, K.O., Hamade, T., Raiswell, R., Morris, R.C., Ferris, F.G., Southam, G., and Canfeld, D.E. Could bacteria have formed the Precambrian banded iron formations?: Geology. 2002; 30: 1079–1082, doi:10.1130/0091-7613(2002)030<1079:CBHFTP>2.0.CO;2.

[12] Robb, L. Introduction to Ore-forming Processes. Blackwell publishing. 2005; 373 pp.

[13] Konhauser, K.O., Pecoits, E., Lalonde, S.V., Papineau, D., Nisbet, E.G., Barley, M.E., Arndt, N.T., Zahnle, K., Kamber, B.S. Oceanic nickel depletion and a methanogen famine before the great oxidation event. Nature. 2009; 458:750–753.

[14] Bontognali, T.R.R., Fischer, W.W., Föllmi, K.B. Siliciclastic associated banded iron formation from the 3.2 Ga Moodies Group, Barberton Greenstone Belt, South Africa. Prec. Res. 2013; 226: 116–124.

[15] Beukes, N.J., and Gutzmer, J. Origin and paleoenvironmental significance of major iron formations at the Archean-Paleoproterozoic boundary: Reviews in Economic Geology. 2008; 15: 5–47.

[16] Isley, A. E. and Abbott, D. H. Plume-related mafic volcanism and the deposition of banded iron formation. J. Geophys. Res. 1999; 104:15461–15477.

[17] Bekker, A., Holland, H. D., Wang, P. L., Rumble, I. I. I., Stein, H. J., Hannah, J. L., Coetzee, L. L. and Beukes, N. J. Dating the rise of atmospheric oxygen. Nature. 2004; 427: 117–120.

[18] Mukhopadhyay, J., Crowley, Q. G., Ghosh, S., Ghosh, G., Chakrabarti, K., Misra, B., Heron, K. and Bose, S. Oxygenation of the Archean atmosphere: New paleosol constraints from eastern India. Geology. 2014; 42: 923–926.

[19] Canfield, D.E., A new model for Proterozoic ocean chemistry. Nature. 1998; 396: 450–453.

[20] Kump, L. R. and Seyfried, W. E. Jr. Hydrothermal Fe fluxes during the Precambrian: effect of low oceanic sulfate concentrations and low hydrostatic pressure on the composition of black smokers. Earth Planet. Sci. Lett. 2005; 235: 654–662.

[21] Fairchild, I. J. and Kennedy, M. J. Neoproterozoic glaciation in the Earth system. J. Geol. Soc. London. 2007; 164: 895–921.

[22] Rasmussen, B., Fletcher, I. R., Bekker, A., Muhling, J. R., Gregory, C. J. and Thorne, A. M. Deposition of 1.88-

billion-yearold iron formations as a consequence of rapid crustal growth. Nature. 2012; 484: 498–501.

[23] Holland, H. D. The Chemical Evolution of the Atmosphere and Oceans. Prince-ton University Press, Princeton. 1984; 582 p.

[24] Trendall, A. F. The significance of iron-formation in the Precambrian stratigraphic record. In Altermann, W., Corcoran, P. L. (eds.) Precambrian Sedimentary Environments: A Modern Approach to Depositional Systems, volume. 33. International Association of Sedimentologists Special Publication, Blackwell, Oxford. 2002; 33–66.

[25] Huston, D.L., Logan, G.A. Barite, BIFs and bugs: evidence for the evolution of the Earth's early hydrosphere," Earth Planet. Sci. Lett. 2004; 220: 41–55.

[26] Frei, R., Dahl, P. S., Duke, E. F., Frei, K. M., Hansen, T. R., Frandsson, M. M. and Jensen, L. A. Trace element and isotopic characterization of Neoarchean and Paleoproterozoic iron formations in the Black Hills (South Dakota USA): assessment of chemical change during 2.9–1.9 Ga deposition bracketing the 2.4–2.2 Ga first rise of atmospheric oxygen. Prec. Res. 2008; 162: 441–474.

[27] Holland, H.D. Sedimentary mineral deposits and the evolution of Earth's nearsurface environments: Economic Geology and the Bulletin of the Society of Economic Geologists. 2005; 100: 1489–1509, doi:10.2113/gsecongeo .100.8.1489.

[28] Cloud Jr., P.E. Atmospheric and hydrospheric evolution on the primitive earth: both secular accretion and biological and geochemical processes have affected earth's volatile envelope. Science. 1968; 160: 729–736.

[29] Holland, H.D. Ocean-possible source of iron in iron formations. Economic Geology. 1973; 68: 1169-1172. doi:10.2113/gsecongeo.68.7.1169

[30] Bekker, A., Planavsky, N.J., Krape, B., et al., Iron formations: their origins and implications for ancient seawater chemistry, in Treatise on GHeochemiostry. Second ed. Vol. 9: Sediments, Diagenesis, and Sedimentary rocks, Amsterdam: Elsevier. 2014; pp. 561-628.

[31] Bau, M., Möller, P. Rare earth element systematics of the chemicallyprecipitated component in Early Precambrian iron-formations and theevolution of the terrestrial atmosphere–hydrosphere–lithosphere system.Geochim. Cosmochim. Acta. 1993; 57: 2239–2249.

[32] Hamade, T., Konhauser, K.O., Raiswell, R., Goldsmith, S., Morris, R.C. Using Ge/Si ratios to decouple iron and silica fluxes in Precambrian banded iron formations. Geology. 2003; 31: 35–38.

[33] Hagemann, S. G., Angerer, T., Duuring, P., Rosiere, C. A., Figueiredo e Silva, R. C., Lobato, L., Hensler, A. S. and Walde, D. H. G. BIF-hosted iron mineral system: A review. Ore Geol. Rev. 2016; 76: 317–359.

[34] Beukes, N. J., Gutzmer, J. and Mukhopadhyay, J. The Geology and Genesis of High-Grade Hematite Iron Ore Deposits. In Proceedings of Iron Ore. 2002; 23–29.

[35] Spier, C. A., de Oliveira, S. M. B., Sial, A. N., Rosière, C. A. and Ardisson, J. D. Mineralogy and trace-element geochemistry of the high-grade iron ores of the Aguas Claras mine and comparison with the Capão Xavier and Tamanduá iron ore deposits, Quadrilátero Ferrífero, Brazil. Miner. Deposita. 2008 ; 43: 229–254.

[36] Rosière, C. A. and Rios, F. J. The origin of hematite in high grade iron ores based on infrared microscopy and fluid inclusion studies: The example of the Conceição mine, Quadrilátero Ferrífero, Brazil. Econ. Geol. 2004; 99: 611–624.

[37] Suh, C. E., Cabral, A., Shemang, E. M., Mbinkar, L. and Mboudou, G. G. M. Two contrasting iron-ore deposits in the Precambrian mineral belt of Cameroon, West Africa. Explor. Min. Geol. 2008; 17: 197–207.

[38] Suh, C.E., Cabral, A.R., Ndime, E. Geology and ore fabric of the Nkout high-grade haematite deposit, southern Cameroon. In: Proceedings of the 10th Biennal of Smart Science for Exploration and Mining. 2009; pp. 558–560.

[39] Nforba, M.T., Kabeyene, K.V., Suh, C.E. Regolith geochemistry and mineralogy of the Mbalam itabirite-hosted iron ore district, southeastern Cameroon. Open J. Geol. 2011; 1: 17–36.

[40] Chombong N.N., Suh C.E. 2883 Ma commencement of BIF deposition at the northern edge of Congo craton, southern Cameroon: new zircon SHRIMP data constraint from metavolcanics. Episodes. 2013; 36: 47-57.

[41] Ndime, E.N., Ganno, S., Soh Tamehe, L., Nzenti, J.P. Petrography, lithostratigraphy and major element geochemistry of Mesoarchean metamorphosed banded iron formation-hosted Nkout iron ore deposit, north western Congo craton, Central West Africa. J. Afr. Earth Sci. 2018; 148.

[42] Ganno, S, D. Tsozué, Gus Djibril K. N, Milan S .Tchouatcha, Timoléon Ngnotué, Ruth G. Takam and J.P, Nzenti. Geochemical constraints of iron from the

Archaen Ntem Complex (Congo Craton) in the Meyomessi Area, Southern Cameroon. Resource Geology. 2018; DOI: 10.1111/rge. 12172

[43] Ilouga, D.C.I., Suh, C.E., Ghogomu, R.T. Textures and rare earth elements composition of banded iron formations (BIF) at Njweng, Mbalam iron ore district, southern Cameroon. Int. J. Geosci. 2013; 4: 146–165.

[44] Tessontsap Teutsong, Tomaso, R.R., Bontognali, Ndjigui, P.D., Vrijmoed, Teagle, D., Cooper, M., Vance, D. Petrography and geochemistry of the Mesoarchean Bikoula banded iron formation in the Ntem complex (Congo craton), southern Cameroon: implications for its origin. Ore Geol. 2017; 80: 267–388.

[45] Ganno, S., Ngnotue, T., Kouankap, N. G. D., Nzenti, J. P. and Notsa, F. M. Petrology and geochemistry of the banded iron-formations from Ntem complex greenstones belt, Elom area, southern Cameroon: Implications for the origin and depositional environment. Chem. Erde-Geochem. 2015a; 75: 375–387.

[46] Ganno, S., Moudioh, C., Nzina Nchare, A., Kouankap Nono, G. D. and Nzenti, J. P. Geochemical fingerprint and iron ore potential of the siliceous itabirite from Palaeoproterozoic Nyong series, Zambi area, southwestern Cameroon. Resour. Geol. 2015b; 66: 71–80.

[47] Ganno, S., Njiosseu, T. E. L., Kouankap, N. G. D., Djoukouo, S. A. P., Moudioh, C., Ngnotué, T. and Nzenti, J. P. A mixed seawater and hydrothermal origin of superior-type banded iron formation (BIF)-hosted Kouambo iron deposit, Palaeoproterozoic Nyong series, southwestern Cameroon: Constraints from petrography and geochemistry. Ore Geol. Rev. 2017; 80: 860–875.

[48] Soh Tamehe, L., Nzepang, T.M., Chongtao, W., Ganno, S., Ngnotue, T., Kouankap, N.G.D., Simon, S.J., Zhang, J., Nzenti, J.P. Geology and geochemical constrains on the origin and depositional setting of the Kpwa–Atog Boga banded iron formations (BIFs), northwestern Congo craton, southern Cameroon. Ore Geol. Rev. 2018; 95: 620–638.

[49] Sikaping, S. Métamorphisme et minéralisations associées du secteur de Gouap–Nkolo (Région du Sud) Unpublished Master thesis. University of Yaounde. 2012 ; pp. 77.

[50] Soh, L Tamehe, W. Chongtaoa, S. Ganno, J.S. Shaamu, G.D.Kouankap Nono, J.P. Nzenti, Y.B. Lemdjoue, L. Naing Htun. Geology of the Gouap iron deposit, Congo craton, southern Cameroon: Implications for iron ore exploration," Geology Reviews. 2019; 107: 1097–1128, https://doi.org/10.1016/j.oregeorev.2019.03.034

[51] Ndema Mbongué, J.L., Luku, O. Inyogen. Geology and geochemistry of Messondo banded iron formation-hosted iron ore from the northwestern Congo Craton, southern Cameroon: implication for iron ore deposits. GSJ. 2020; 8(2): 4684-4699.

[52] Nzepang Tankwa, M., Ganno, S., Olngbenga Akindeji Okunlola., Tanko Njiosseu, E.L., Soh Tamehe L., Kamguia Woguia, B., Motto Mbita, A.S., & Nzenti, J.P. Petrogenesis and tectonic setting of the Paleoproterozoic Kelle Bidjoka iron formations, Nyong group greenstone belts, southwestern Cameroon. Constraints from petrology, geochemistry, and LA-ICP-MS zircon U-Pb geochronology, International Geology Review. 2020; DOI: 10.1080/00206814.2020.1793423

[53] Moudioh, C., Soh Tamehe, L., Ganno, Sylvestre., Nzepang Tankwa, M., Soares, M.B., Ghosh, R.. Kankeu, Boniface. Nzenti J.P. Tectonic setting of the Bipindi greenstone belt, northwest Congo craton, Cameroon: Implications on BIF deposition. Journal of African Earth Sciences 2020; 171: 103971.

[54] Ilouga D. C. I., Ndong Bidzang F., Ziem A Bidias L. A., Olinga J. B., Tata E., Minyem D Geochemical Characterization of a Stratigraphic Log Bearing Iron Ore in the Sanaga Prospect, Upper Nyong Unit of Ntem Complex, Cameroon. Journal of Geosciences and Geomatics. 2017; 5(5): 218-228. DOI:10.12691/jgg-5-5-1

[55] Mbang Bonda, B. M., Etame, J., Kouske, A. P., Bayiga, E. C., Ngon Ngon, G. F., Mbaï, S. J. Gérard, M. Ore Texture, Mineralogy and Whole Rock Geochemistry of the Iron Mineralization from Edea North Area, Nyong Complex, Southern Cameroon: Implication for Origin and Enrichment Process. International Journal of Geosciences. 2017; 8: 659-677. https://doi.org/10.4236/ijg.2017.85036

[56] Ndema Mbongué, J.L and Aroke E. Alemnju. Petrology and Geochemical Constraints on the Origin of Banded Iron Formation-Hosted Iron Mineralization from the Paleoproterozoic Nyong Serie (Congo Craton, South Cameroon), Pout Njouma Area (Edea North): Evidence for Iron Ore Deposits. International Journal of Research and Innovative in Applied Science (IJRIAS). 2020; 5(8): 55-72.

[57] Nkoumbou, C. Fuh Calistus, Jacqueline Tchakounte Numbem a, Yolande Vanessa Belle Ekwe Lobe´, Christin Steve Nwagoum Keyamfe Petrology and geochemistry of REE-rich Mafe´ banded

ironformations (Bafia group, Cameroon). Comptes Rendus Geoscience. 2017; 349: 165–174.

[58] Nzenti JP, Barbey P, Macaudiere J and Soba D. Origin and evolution of the late Precambrian high-grade Yaounde gneisses (Cameroon). Prec Res. 38:91-109.

[59] Toteu S.F., Van Schmus W.R., Penaye J., Nyobé J.B. (1994). U-Pb and Sm-Nd evidence for Eburnean and Pan-African highgrade metamorphism in cratonic rocks of southern Cameroon, Precamb. Res. 1988; 67: 321-347.

[60] Tchameni, R., Mezger, K., Nsifa, N. E. and Pouclet, A. Crustal origin of early Proterozoic syenites in the Congo Craton (Ntem complex), South Cameroon. Lithos. 2001; 57: 23–42.

[61] Shang, C. K., Liégeois, J. P., Satir, M., Frisch, W. and Nsifa, E. N. Late Archaean high-K granite geochronology of the northern metacratonic margin of the Archaean Congo craton, southern Cameroon: Evidence for Pb-loss due to nonmetamorphic causes. Gondwana Res. 2010; 18: 337–355.

[62] Ndema Mbongué JL, Nzenti JP, Cheo E.S. Origin and evolution of the formation of the Nyong serie in the Western Border of the Congo Craton. J Geosci Geom. 2014; 2(2): 62-75.

[63] Ndema Mbongué Jean Lavenir, Sigué Cyrille, Nzenti Jean Paul, and Cheo Emmanuel Suh. Structural Characterization of Outcrop-Scale in Edea and Eseka Area: Evidence for a Complex Polyphase Deformation in the Paleoproterozoic Nyong Serie (Congo craton-South Cameroon). IOSR Journal of Applied Geology and Geophysics (IOSR-JAGG). 2019; 7(5): 01-09.

[64] Nsifa, N. E., Tchameni, R., Nédélec, A., Siqueira, R., Pouclet, A., Bascou, J. Structure and petrology of Pan-African nepheline syenites from the South West Cameroon; Implications for their emplacement mode, petrogenesis and geodynamic significance. Journal of African Earth Sciences. 2013; 87: 44–58.

[65] Maurizot P, Abessolo A, Feybesse JL, Johan V, Lecomte P. Etude et prospection miniere du Sud-Ouest Cameroun. Synthese des travaux de 1978 à 1985. Rapport BRGM. 1986 ; 85 CMR 066.

[66] Delhal, J. et Ledent, D. Musée Royal Afrique Centrale. Tervuren. Rapport. Annuel. 1974 ; pp. 71-76.

[67] Lasserre M, and Soba D. Age liberien des granodiorites et des gneiss a pyroxenes du Cameroun meridional. Bulletin du BRGM. 1976; 2: 17–32.

[68] Lerouge C, Cocherie A, Toteu S.F., Penaye J., Milési J.P., Tchameni R., Nsifa E.N., Fanning C.M., Doloule E. Shrimps UPb zircon age evidence for Paleoproterozoic sedimentation and 2.05Ga syntectonic plutonism in the Nyong Group, SouthWestern Cameroon: consequences for the Eburnean-Transamazonian belt of NE Brazil and Central Africa. J Afr Earth Sci. 2006; 44: 413-427.

[69] Pouclet A, Tcahameni R, Mezger K, Vidal M, Nsifa EN, Shang C and Penaye J. Archaean crustal accretion at the Northern border of Congo Craton (South Cameroon): The charnockite-TTG ling. Bull. Soc. Géol. France. 2007; 178: 331-342.

[70] Ebah Abeng, S.A.E., Ndjigui, P.D., Beyanu, A.A., Teutsong, T., Bilong. P. Geochemistry of pyroxenites, amphibolites and their weathered products in the Nyong unit, SW Cameroon (NW border of Congo Craton): Implications for Au-PGE exploration. Journal of Geochem. Expl. 2012; 114: 1-19.

[71] Siivola, J. and Schmid, R. List of Mineral Abbreviations. Recommen-dations by the IUGS Subcommission on the Systematics of Metamor-phic Rocks 2007; Web version 01.02.2007; www.bgs.ac.uk.scmr/home.html

[72] Actlabs. Schedule of Services and Fees, Geochemistry – International. 2019.

[73] Ewers, W.E., Morris, R.C. Studies of the Dales George member of the Brockman Iron Formation, Western Australia. Econ. Geol. 1981; 76: 1929–1953.

[74] Pearce, J.A. Role of the sub-continental lithosphere in magma genesis at active continental margins, in: Hawkesworth C.J and Norry M.J (eds), Continental baslts and mantle xenoliths, Shiva, Nantwich. 1983; p. 230-249.

[75] Dymek, R.F., Klein, C. Chemistry, petrology and origin of banded iron formation lithologies from 3800 Ma Isua supracrustal belt, West Greenland. Precambrian Res. 1988; 39: 247–302.

[76] Arora, M., Govil, P.K., Charan, S.N., Uday Raj, B., Balaram, V., Manikyamba, C., Chatterjee, A.K., Naqvi, S.M. Geochemistry and origin of Archean banded iron–formation from the Bababudan Schist Belt, India. Econ. Geol. 1995; 90: 2040–2057.

[77] Gross G. A. and Macleod, C. R. A Preliminary Assessment of the Chemical Composition of Iron-Formations in Canada. Canadian Mineralogist. 1980; 18: 223-229.

[78] Gross, G. A. "Geochemistry of Iron-Formation in Canada," In: J.-J. Chauvel, C. Yugi, E. M. El-Shazly, G. A. Gross, K. Laajoki, M. S. Markov, K. L. Rai, V. A. Stulchikov and S. S. Augustithis Eds., Ancient Banded

iron Formations (Regional Representations), Theophrastus, Athens. 1990; pp. 3-26.

[79] Adekoya, A.J.,Okonkwo, C.T. andAdepoju,M.O. Geochemistry of Muro Banded Iron Formation, Central Nigeria. Int. J. Geosci. 2012; 3:1074–1083.

[80] Sciuba M. Mineralogy and Geochemistry of the Banded Iron-Formation in the Svartliden Gold Deposit, Northern Sweden. 2013.

[81] Stanton, R.LOre petrology. London and New York (McGraw-Hill Book Co.). 1972; Xviii + 713pp. 242 figs.

[82] Alibert, C., McCulloch, M.T. Rare earth element and Nd isotopic compositions of the BIFs and associated shales from Hamersley, Western Australia. Geochimica et Cosmochimica. Acta. 1993; 57: 187–204.

[83] Bau, M., Dulski, P. Distribution of yttrium and rare-earth elements in the Penge and Kuruman Iron Formation, Transvaal Supergroup, South Africa. Precambrian Research. 1996; 79; 37–55.

[84] Akagi, T. and Masuda, A. A simple thermodynamic interpretation of Ce anaomaly. Chemical Journal. 1998; 35(5): 301-314.

[85] Taylor, S. R. and McLennan, S. M. The continental crust: its composition and evolution. Blackwell Publishing, Oxford, UK. 1985; p. 312.

[86] Chombong, N.N., Suh, C.E., Lehmann, B., Vishiti, A., Ilouga, D.C., Shemang, E.M., Tantoh, B.S., Kedia, A.C. Host rock geochemistry, texture and chemical composition of magnetite in iron ore in the Neoarchaean Nyong unit in southern Cameroon. Appl. Earth Sci. 2017; http://dx.doi.org/10.1080/03717453.2017.1345507.

[87] Anderson, K.F.E., Frances, W., Rollinson, G.K., Charles, J.M. Quantitative mineralogical and chemical assessment of the Nkout iron ore deposit, Southern Cameroon. Ore Geol. Rev. 2014; 62: 25–39.

[88] Manikyamba, C., Balaram, V., and Naqvi, S.M. Geochemical signatures of polygenetic origin of a banded iron formation (BIF) of the Archaean Sandur greenstone belt (schist belt) Karnataka nucleus, India, Precambrian Research. 1993; 61: 137-164.

[89] Gnaneswar Rao, T., Naqvi, S.M. Geochemistry, depositional environment and tectonic setting of the BIF of late Archaean setting of the BIF of late Archaean Chitradurga schist belt, India. Chemical Geology. 1995; 121: 217–243.

[90] Klein, C., and Ladeira, E.A. Geochemistry and Petrology of some Proterozoic BIF of the Quadrilatero Ferrifero, Minas Gerais, Brazil, Economic Geology. 2000; 95: 405-428.

[91] Rollinson, H.R. Using geochemical data: evaluation, presentation, interpretation, Pearson edition. 1993 ; 352 p.

[92] Bonnot-Courtois. C. Distribution des terres rares dans les dépôts hydrothermaux de la zone Famous et des Galapagos – Comparaison avec les sédiments métallifères. Marine Geology. 1981 ; 39: 1-14.

[93] James, H.J. Sedimentary Facies of Iron Formation. Economic Geology. 1954; 49: 235-293. https://doi.org/10.2113/gsecongeo.49.3.235

[94] James H.L. Chemistry of the iron-rich sedimentary rocks, In: Fleischer M. (ed.), Data of Geochemistry', 6th edition, Paper 440-W, U.S. Govt. Printing Office, Washington D.C. 1966.

[95] James, H.L. Precambrian iron-formations: Nature, origin, and mineralogic evolution from sedimentation to metamorphism. In: Wolf, K.H., Chilingarian, G.V. (Eds.), Diagenesis III: Developments in Sedimentology. 1992; 47: 543–589.

[96] Cox, R., Lowe, D.R., Cullers, R.L. The influence of sediment recycling and basement composition on evolution of mudrock chemistry in the south-western United States. Geochim. Cosmochim. Acta. 1995; 59: 2919–2940.

[97] Girty, G.H., Ridge, D.L., Knaack, C., Johnson, D., Al-Riyami, R.K. Provenance and depositional setting of Paleozoic chert and argillite, Sierra Nevada, California. J. Sediment. Res. 1996; 66: 107–118.

[98] ] Herron, M.M. (1988). Geochemical classification of terrigenous sands and shales from core or log data. J. Sediment. Petrol. 58, 820–829.

[99] Floyd, P.A., Winchester, J.A., Park, R.G. Geochemistry and tectonic setting of lewisian clastic metasediments from the early proterozoic loch maree group of gairloch. N.W. Scotland. Precambrian Res. 1989; 45 (1–3): 203–214.

[100] Govett, G.J.S. Origin of Banded Iron-Formation. Geological Society of America Bulletin 1966; 77: 1191-1212.

[101] Lepp, H. and Goldich, S.S. Origin of the Precambrian Iron-Formation. Economic Geology. 1964; 59:1025-1060. https://doi.org/10.2113/gsecongeo.59.6.1025

[102] Roser, B.P., Korsch, R.J. Determination of tectonic setting of sandstone–mudstone suites using $SiO_2$ content and $K_2O/Na_2O$ ratio. J. Geol. 1986; 94: 635–650.

[103] Wright, J., Schrader, H. and Holser, W. Paleoredox variations in ancient oceans recorded by rare earth elements in fossil apatite. Geochim. Cosmochim. Acta. 1987; 51: 631–644.

[104] Isley, A.E. Hydrothermal plumes and the delivery of iron to banded iron formations. Journal of Geology. 1995; 103: 169-185. doi:10.1086/629734

[105] Frei, R., Polat, A. Source heterogeneity for the major components of 3.7 Ga banded iron formation (Isua Greenstone Belt, western Greenland): tracing the nature of interacting water masses in BIF formation. Earth Planet. Sci. Lett. 2007; 253: 266–281.

[106] Belevtsev, Y. N., Belevtsev, R. Y. and Siroshtan, R. I. The Krivoy Rog Basin. In Trendall, A. F., Morris, R. C. (eds.) Ironformation: Facts and Problems. Elsevier, Amsterdam. 1982; 211–252.

[107] Cloud, P. Paleoecological significance of banded iron-formation. Economic Geology. 1973; 68; 1135−1143.

[108] Bonatti, E. Metallogenesis at oceanic spreading centers. Annu. Rev. Earth and Planet. Sci. 1975; 3: 401–433.

[109] Toth, J.R. Deposition of submarine crusts rich in manganese and iron. GSA Bull. 1980; 91 (1): 44–54.

[110] Marchig, V., Gundlach, H., Möller, P., Schley, F. Some geochemical indicatorsfor discrimination between diagenetic and hydrothermal metalliferoussediments. Mar. Geol. 1982; 50: 241–256.

[111] Lan, T.G., Fan, H.R., Santosh, M., Hu, F.F., Yang, K.F., Liu, Y.S. U-Pb zircon chronology, geochemistry and isotopes of the Changyi banded iron formation in the eastern Shandong Province: constraints on BIF genesis and implications for Paleoproterozoic tectonic evolution of the North China Craton. Ore Geol. Rev. 2014; 56: 472–486.

[112] Barrett, T.J. Chemistry and mineralogy of Jurassic bedded chert overlyingophiolites in the North Appenines, Italy. Chem. Geol. 1981; 34: 289–317.

[113] Danielson, A., Moller, P., Dulski, P. The europium anomalies in banded iron formations and the thermal history of the oceanic crust. Chem. Geol. 1992; 97: 89–100.

[114] Bau, M., Dulski, P. Comparing yttrium and rare earths in hydrothermal fluids from the Mid-Atlantic Ridge: implications for Y and REE behaviour during nearvent mixing and for the Y/Ho ratio of Proterozoic seawater. Chem. Geol. 1999; 155: 77–90.

[115] Alexander, B.W., Bau, M., Andersson, P., Dulski, P. Continentally-derived solutes in shallow Archean seawater: rare earth element and Nd isotope evidence in iron formation from the 2.9 Ga Pongola Supergroup, South Africa. Geochim. Cosmochim. Acta. 2008; 72: 378–394.

[116] Gourcerol, B., Thurston, P.C., Kontak, D.J., Côté-Mantha, O., and Biczok, J. Depositional setting of Algoma-type banded iron formation: Precambrian Research. 2016; 281: p. 47–79. 10.1016/j.precamres.2016,04.019

[117] Thurston, P.C., Kamber, B.S., Whitehouse, M. Archean cherts in banded iron formation: insight into Neoarchean ocean chemistry and depositional processes. Precambr. Res. 2012; 214–215, 227–257.

[118] Alibo, D.S., Nozaki, Y. Rare earth elements in seawater: particle association, shale normalization, and Ce oxidation. Geochimica et Cosmochimica Acta. 1999; 63: 363–372.

[119] Angerer, T., Hagemann, S. G. and Danyushevsky, L. V. Geochemical evolution of the banded iron formation-hosted high-grade iron ore system in the Koolyanobbing Greenstone Belt, Western Australia. Econ. Geol. 2012; 107: 599–644.

[120] Belevtsev, Y. N., Kravchenko, V. M., Kulik, D. A., Belevtsev, R. Y., Borisenko, V. G., Drozdovskaya, A. A., Epatko, Y. M., Zankevich, B. A., Kalinichenko, O. A., Koval, V. B., Korzhnev, M. N., Kusheyev, V. V., Lazurenko, V. I., Litvinskaya, M. A., Nikolayenko, V. I., Pirogov, B. I., Prozhogin, L. G., Pikovskiy, E. S., Samsonov, V. A., Skvortsov, V. V., Savchenko, L. T., Stebnovskaya, Y. M., Tereshchenko, S. I., Chaykin, S. I. and Yaroshchuk, M. A. (Precambrian banded iron formations of the European part of the USSR. Genesis of iron-ores. Naukova Dumka Press, Kiev, Ukrainia (IGCP UNESCO Project. 1991; No 247 (in Russian)).

[121] Li, H. M., Zhang, Z. J., Li, L. X., Zhang, Z. C., Chen, J. and Yao, T. Types and general characteristics of the BIFrelated iron deposits in China. Ore Geol. Rev. 2014; 57: 264–287.

[122] Guider, J. W. Iron ore beneficiation -key to modern steelmaking. Mineral. Engineering. 1981; 33: 410–413.

[123] Dobbins, M. S. and Burnet, G. Production of an iron ore concentrate from the iron-rich fraction of power plant fly ash. Resour. Conserv. 1982; 9: 231–242.